

A Systematic Study on the Resonance in Collisional Neutrino Flavor Instability

Jiabao Liu,¹ Masamichi Zaizen,² and Shoichi Yamada^{3,4}

¹*Department of Physics and Applied Physics, School of Advanced Science and Engineering, Waseda University, Tokyo 169-8555, Japan*

²*Faculty of Science and Engineering, Waseda University, Tokyo 169-8555, Japan*

³*Department of Physics, School of Advanced Science and Engineering, Waseda University, Tokyo 169-8555, Japan*

⁴*Research Institute for Science and Engineering, Waseda University, Tokyo 169-8555, Japan*

(Dated: February 14, 2023)

Investigations on the resonance in the collisional flavor instability (CFI) of neutrinos, which were reported recently, are reported. We show that the resonance occurs not only for the isotropy-preserving modes as pointed out in the previous work but also for the isotropy-breaking modes and that it enhances the growth rate of CFI by orders of magnitude. Employing the linear analysis and nonlinear numerical simulations in the two-flavor scheme and under the relaxation approximation for the collision term, we discuss the criterion for the resonance, its effect on the nonlinear evolution as well as the influences of homogeneity-breaking ($k \neq 0$) perturbations as well as of anisotropy in the background on the resonance. We will also touch the cohabitation of the resonance with the fast flavor conversion (FFC).

I. INTRODUCTION

Neutrino flavor oscillations, particularly the fast flavor conversion (FFC), have been studied extensively these days due to their more rapid growth compared to the other conversion modes[1–6]. The neutrino-flavor-lepton-number (NFLN) crossing, that is, the situation in which one flavor is dominant over the other in certain momentum directions while the opposite is true in other directions at least for a pair of neutrino flavors, is known to be the criterion for FFC[7]. In its application to core-collapse supernovae (CCSNe), the electron-lepton-number (ELN) crossing has been conveniently searched for in many papers[8–18], since other flavor-lepton-numbers are normally much smaller. The ordinary non-forward scatterings of neutrinos were once thought to destroy the coherence among neutrinos, thus, working against the neutrino flavor oscillations. The interplay between FFC and the ordinary collisions has been investigated from various directions[19–26]. Interestingly, some numerical simulations, in which the collision rate was artificially modified by orders of magnitudes, found that FFC can be enhanced by the collisions[22]. It was also pointed out that the collisions may modify the neutrino spectra so that FFC could be driven[27]. The so-called collisional dilemma, i.e., enhancement or damping of FFC by the ordinary collision, has not been fully resolved so far.

Recently the existence of a new type of flavor conversion referred to as the collisional flavor instability (CFI), which is driven by the collisions themselves and can occur without the NFLN crossing and hence FFC, was pointed out[28]. It was also shown that the onset of CFI could be hastened by FFC[29]. For homogeneous, isotropic, and monochromatic neutrino distributions the condition for CFI is thought to be that the collision rate for neutrino should be different from that for antineutrino[28]. The existence of CFI was

later confirmed numerically for homogeneous, isotropic but non-monochromatic neutrino distributions[30]. The authors added to the criterion for CFI a condition that there exists at least one ELN crossing in neutrino *energy*.

In the following sections, we derive the exact linear growth rate of the CFI mode with $k = 0$ at the resonance peak based on the dispersion relation for the homogeneous, isotropic and monochromatic neutrino distributions in the background and give the criterion for the resonance as well. We consider not only the isotropy-preserving mode but also the isotropy-breaking mode, which has been somehow overlooked in the literature so far, and demonstrate that they also give rise to the resonance. For the isotropy-preserving mode, on the other hand, we solve the QKE numerically in the resonance region and study the nonlinear evolution of the resonance. We show that the saturation is reached more rapidly in that case but that the saturation level is hardly affected.

We then proceed to the non-monochromatic case. We adopt the Fermi-Dirac distribution for the neutrino energy. Numerically evaluating the dispersion relation, we find that the growth rate and the resonance criterion obtained in the monochromatic case remain good approximations if the monochromatic collision rates are simply replaced by the mean collision rates. Finally, the effect of non-vanishing wave numbers ($k \neq 0$) in the perturbation or of the anisotropy in the background angular distributions in momentum space is studied again based on the dispersion relation. It is found that they both tend to suppress CFI. We also touch the case, in which the ELN crossing is present initially and the FFC coexists with the CFI resonance.

II. DISPERSION RELATION

The neutrino flavor content in the two flavor approximation is described by the neutrino flavor density matrix

$$\rho(x, P) = \begin{pmatrix} f_{\nu_e} & S \\ S^* & f_{\nu_x} \end{pmatrix}, \quad (1)$$

where the star means the complex conjugate; the diagonal elements are neutrino occupation numbers in the individual flavor eigenstates whereas the off-diagonal elements represent the coherence between the two flavors; $x = (x^\mu)$ is the spacetime position and $P = (E, \mathbf{v})$ is the 4-momentum vector of neutrinos, in which neutrinos are assumed to be ultra-relativistic particles traveling at the speed of light $|\mathbf{v}| = 1$ in natural units. We use the signature convention of $\eta_{\mu\nu} = \text{diag}(+1, -1, -1, -1)$ for the Minkowski metric in this paper. In the flavor isospin convention, negative energy $E < 0$ stand for antineutrinos as $\rho(E) = -\bar{\rho}(-E)$. Antineutrino quantities are indicated by the bar.

The evolution of the flavor density matrix is described by the quantum kinetic equation

$$i\mathbf{v} \cdot \partial \rho = [H, \rho] + iC, \quad (2)$$

where H is the Hamiltonian and C is the collision term. The Hamiltonian has the vacuum, matter and neutrino

contributions given as Here the terms are expressed as

$$\begin{aligned} H &= H_{\text{vac}} + H_{\text{mat}} + H_\nu, \\ H_{\text{vac}}(x, P) &= \frac{M^2}{2E}, \\ H_{\text{mat}}(x, P) &= \sqrt{2}G_{\text{F}}v \cdot \text{diag}(j_e(x), j_x(x)), \\ H_\nu(x, P) &= \sqrt{2}G_{\text{F}}v \cdot \int dP' \rho(x, P')v', \end{aligned} \quad (3)$$

where M^2 is the neutrino mass-squared matrix; $j_\alpha(x)$ is the lepton number 4-current of the charged lepton species α ; the integral over 4-momentum is abbreviated as

$$\int dP = \int_{-\infty}^{\infty} \frac{E^2 dE}{2\pi^2} \int \frac{d\mathbf{v}}{4\pi}. \quad (4)$$

The collision term C can be written for neutrinos in relaxation approximation as

$$C(x, P) = \frac{1}{2} \{ \text{diag}(\Gamma_e(x, P), \Gamma_x(x, P)), \rho_{\text{eq}} - \rho \}, \quad (5)$$

where the curly bracket denotes anti-commutator; $\Gamma_\alpha(x, P)$ is the collision rate for the charged lepton α ; ρ_{eq} is the equilibrium state that is approached through the collision. The collision term for antineutrinos is written in the same manner.

The quantum kinetic equation 2 can be linearized with respect to S if $|S| \ll f_i$ as

$$v \cdot (\partial - \Lambda_{0e} + \Lambda_{0x})S_{ex} + (f_{\nu_e} - f_{\nu_x})\sqrt{2}G_{\text{F}} \int dP' v \cdot v' S_{ex}(P') + \frac{1}{2E} \sum_{z=e,x} (M_{ez}^2 S_{zx} - S_{ez} M_{zx}^2) + i\Gamma_{ex} S_{ex} = 0, \quad (6)$$

where $\Lambda_{0z} = \sqrt{2}G_{\text{F}}[j_z(x) + \int dP f_{\nu_z}(x, P)v]$ and $\Gamma_{ex}(E) = [\Gamma_e(E) + \Gamma_x(E)]/2$. Assuming the plane wave solution as usual as

$$S(x, P) = S(k, P)e^{ik \cdot x}, \quad (7)$$

where $k = (\omega, \mathbf{k})$ is the 4-wavevector and ignoring the vacuum term which is important for the slow instabilities[31], but plays a minor role to give initial perturbations for the fast instability, we obtain

$$\{v \cdot (k - \Lambda_{0e} + \Lambda_{0x}) + i\Gamma_{ex}\}S_{ex} + (f_{\nu_e} - f_{\nu_x})v \cdot a = 0. \quad (8)$$

where the vector a is defined as

$$a = \sqrt{2}G_{\text{F}} \int dP S_{ex}(P)v. \quad (9)$$

Then S can be solved as

$$S_{ex}(k, P) = -\frac{(f_{\nu_e} - f_{\nu_x})v \cdot a}{v \cdot (k - \Lambda_{0e} + \Lambda_{0x}) + i\Gamma_{ex}}. \quad (10)$$

Substitution of this expression back into the definition of a in Eq.9 leads to the following homogeneous equation:

$$\Pi_{ex}(k)a_{ex}(k) = 0, \quad (11)$$

where the matrix Π_{ex} is defined as

$$\Pi_{ex}(k) = \eta + \sqrt{2}G_{\text{F}} \int \frac{dP (f_{\nu_e} - f_{\nu_x})v \otimes v^\top}{v \cdot (k - \Lambda_{0e} + \Lambda_{0x}) + i\Gamma_{ex}}. \quad (12)$$

Λ 's in the denominator may be absorbed into k , shifting the real part of k alone and unaffected the instability[32]. Note that the so-called zero mode with $k = 0$ does not mean a mode homogeneous in space after this shift. In the isotropic case, which we consider throughout this paper, the neutrino contribution to the shift vanishes.

Nontrivial solutions of a exist if and only if

$$\det \Pi_{ex}(k) = 0, \quad (13)$$

which gives us the dispersion relation $\omega = \omega(\mathbf{k})$. The positive imaginary part of ω , $\text{Im}\omega > 0$, implies that the flavor eigen state is unstable and the perturbation in S

grows exponentially in time, an indication of CFI. Introducing the spherical coordinates for the neutrino velocity \mathbf{v} , we can write down the matrix Π_{ex} as

$$\Pi_{ex}(k) = \eta + \sqrt{2}G_F \int_{-\infty}^{\infty} \frac{E^2 dE}{2\pi^2} \int_{-1}^1 \frac{dc_\theta}{2} \int_0^{2\pi} \frac{d\phi}{2\pi} \frac{f_{\nu_e}(E, \mathbf{v}) - f_{\nu_x}(E, \mathbf{v})}{\omega - \mathbf{v} \cdot \mathbf{k} + i\Gamma_{ex}(E)} \times \begin{pmatrix} 1 & \sqrt{1-c_\theta^2}c_\phi & \sqrt{1-c_\theta^2}s_\phi & c_\theta \\ \sqrt{1-c_\theta^2}c_\phi & (1-c_\theta^2)c_\phi^2 & (1-c_\theta^2)s_\phi c_\phi & \sqrt{1-c_\theta^2}c_\theta c_\phi \\ \sqrt{1-c_\theta^2}s_\phi & (1-c_\theta^2)s_\phi c_\phi & (1-c_\theta^2)s_\phi^2 & \sqrt{1-c_\theta^2}c_\theta s_\phi \\ c_\theta & \sqrt{1-c_\theta^2}c_\theta c_\phi & \sqrt{1-c_\theta^2}c_\theta s_\phi & c_\theta^2 \end{pmatrix}, \quad (14)$$

where the following abbreviations are used: $c_\theta = \cos(\theta)$, $s_\theta = \sin(\theta)$, $c_\phi = \cos(\phi)$, $s_\phi = \sin(\phi)$.

The expression is significantly simplified if the background neutrino is isotropic in momentum space. In fact for $k = 0$, Π_{ex} becomes even simpler, being diagonal. The equation to be solved is reduced in this case to

$$I = \sqrt{2}G_F \int_{-\infty}^{\infty} \frac{E^2 dE}{2\pi^2} \frac{f_{\nu_e}(E) - f_{\nu_x}(E)}{\omega + i\Gamma_{ex}(E)} = -1, 3. \quad (15)$$

Note that the solutions for $I = 3$ are degenerate with the multiplicity of 3. The solutions of Eq.15 are collectively referred to as the homogeneity-preserving modes although the wave vector is shifted. It should be noted that only the solution branch for $I = -1$ has

been studied in previous papers[30][33]. This is because the authors of these papers assumed tacitly that the perturbation is isotropic. In fact, the spatial components of a vanish in that case so that the three spatial components of Eq.11 become trivial. This is equivalent to ignoring the modes for $I = 3$. If one allows anisotropic perturbations instead, the spatial components of a become nonzero and the solution branch for $I = 3$ is recovered. For this reason, we call the solution branch for $I = -1$ the isotropy-preserving branch and refer to the solution for $I = 3$ as the isotropy-breaking branch.

The analysis of the real and the imaginary parts of Eq.15 leads to the necessary condition for the occurrence of CFI, i.e., $\text{Im}[\omega] > 0$, that the following function, $F(E)$, of $E(> 0)$,

$$F(E) = [f_{\nu_e}(E) - f_{\nu_x}(E)] [\text{Re}[\omega]^2 + (\text{Im}[\omega] + \bar{\Gamma}_{ex}(E))^2] - [f_{\bar{\nu}_e}(E) - f_{\bar{\nu}_x}(E)] [\text{Re}[\omega]^2 + (\text{Im}[\omega] + \Gamma_{ex}(E))^2] \quad (16)$$

should have at least one zero point, or crossing in energy. When the energy-dependent collision rates, $\Gamma_{ex}(E)$ and $\bar{\Gamma}_{ex}(E)$, are identical for neutrinos and antineutrinos, this condition is reduced to the criterion derived by Lin et al.[30]

III. MONOCHROMATIC NEUTRINOS

A. Exact Solutions in the Linear Analysis

In this section, we consider monochromatic neutrinos and solve Eq.15 analytically. We assume the following background distributions:

$$f_{\nu_e}(E) - f_{\nu_x}(E) = \frac{2\pi^2}{\sqrt{2}G_F E^2} [g\delta(E - \epsilon) - \bar{g}\delta(E + \bar{\epsilon})], \quad (17)$$

where $g, \bar{g}, \epsilon, \bar{\epsilon}$ are model parameters. Then Eq.15 becomes

$$\frac{g}{\omega + i\Gamma} - \frac{\bar{g}}{\omega + i\bar{\Gamma}} = -1, 3, \quad (18)$$

where $\Gamma = \Gamma_{ex}(E = \epsilon)$, $\bar{\Gamma} = \bar{\Gamma}_{ex}(E = -\bar{\epsilon})$. Note that in the typical situation in the supernova core of our concern the neutrino number densities always exceed the collision rates by several orders of magnitude $g, \bar{g} \gg \Gamma, \bar{\Gamma}$, the fact used in the following. Eq.18 can be solved easily to produce

$$\omega_{\pm} = -A - i\gamma \pm \sqrt{A^2 - \alpha^2 + i2G\alpha}, \quad (19)$$

for the isotropy-preserving modes and

$$\omega_{\pm} = \frac{A}{3} - i\gamma \pm \sqrt{\left(\frac{A}{3}\right)^2 - \alpha^2 - i\frac{2}{3}G\alpha}, \quad (20)$$

for the isotropy-breaking modes. In the above equations, the following notations are introduced:

$$G = \frac{g + \bar{g}}{2}, \quad A = \frac{g - \bar{g}}{2}, \quad \gamma = \frac{\Gamma + \bar{\Gamma}}{2}, \quad \alpha = \frac{\Gamma - \bar{\Gamma}}{2}. \quad (21)$$

Note that when the collision rates are identical between neutrino and antineutrino, or $\alpha = 0$, the imaginary part of these mode is $-\gamma < 0$, implying that they are all stable. It follows hence that the inequality of the collision rates is needed for CFI, which was the criterion postulated by Johns[28].

The complex frequencies given in Eqs.19 and 20 are approximated as

$$\omega_{\pm} = \begin{cases} -A - i\gamma \pm \left(|A| + i \frac{G|\alpha|}{|A|} \right), & \text{if } A^2 \gg G|\alpha|, \\ -A - i\gamma \pm \sqrt{i2G\alpha}, & \text{if } A^2 \ll G|\alpha|, \end{cases} \quad (22)$$

for the isotropy-preserving branch and

$$\omega_{\pm} = \begin{cases} A - i\gamma \pm \left(\frac{|A|}{3} - i \frac{1}{3} \frac{G|\alpha|}{|A|} \right), & \text{if } A^2 \gg G|\alpha|, \\ \frac{A}{3} - i\gamma \pm \sqrt{-i \frac{2}{3} G\alpha}, & \text{if } A^2 \ll G|\alpha|, \end{cases} \quad (23)$$

for the isotropy-breaking branch. The results for the isotropy-preserving modes were derived previously in the non-resonance region[28, 30] and in the resonance region[33], whereas those for the isotropy-breaking modes have not been presented so far because the authors assumed isotropy not only for the background but also for perturbations as we mentioned earlier.

We plot the real and imaginary parts of ω for the two branches in Figs. 1 and 2, respectively, for the following parameter values: $g = 1 \text{ cm}^{-1}$, $\gamma = 2.05 \times 10^{-7} \text{ cm}^{-1}$, $\alpha = -4.5 \times 10^{-8} \text{ cm}^{-1}$. In these plots we take \bar{g} as a free parameter. It is apparent from the plots of imaginary part that there is a rather narrow region of \bar{g} , in which the growth rate is enhanced roughly by two orders of magnitude. This is the resonance that Johns et al.[33] first pointed out and we will focus on in this paper. In fact, the resonance occurs near the point, at which the real parts of ω_+ and ω_- come close to each other. Note that although the resonance was reported only for the isotropy-preserving modes in [33], it occurs also for the isotropy-breaking modes as shown in Fig.2.

To locate where the enhancement occurs exactly, we differentiate $\omega_+(g, \bar{g}, \Gamma, \bar{\Gamma})$ of the isotropy-preserving branch in Eq.19 with respect to \bar{g} as

$$\begin{aligned} \frac{\partial \omega}{\partial \bar{g}} &= \frac{1}{2} + \frac{1}{2}(A^2 - \alpha^2 + i2G\alpha)^{-\frac{1}{2}}(-A + i\alpha) \\ &= \frac{1}{2} + \frac{1}{2}|C|^{-\frac{1}{2}} \left[\left(-A \cos \frac{\theta[C]}{2} + \alpha \sin \frac{\theta[C]}{2} \right) + \right. \\ &\quad \left. i \left(\alpha \cos \frac{\theta[C]}{2} - A \sin \frac{\theta[C]}{2} \right) \right], \end{aligned} \quad (24)$$

where we define C as

$$C = A^2 - \alpha^2 + i2G\alpha = |C|e^{i\theta[C]}. \quad (25)$$

The imaginary part of the derivative vanishes at the unique value of \bar{g} that corresponds to $A^2 = \alpha^2$. Thus the resonance occurs when $|A| \approx |\alpha|$, i.e., the number densities of neutrino and antineutrino come close to each other. Note that the difference in the collision rates is usually orders of magnitude smaller than the difference in the number densities, $|\alpha| \ll |A|$.

In the isotropy-preserving branch, the imaginary part of ω_+ is given approximately as

$$\text{Im } \omega_+ \approx \begin{cases} -\gamma + \frac{G|\alpha|}{|A|}, & \text{if } A^2 \gg G|\alpha|, \\ -\gamma + \sqrt{G|\alpha|}, & \text{if } A^2 \ll G|\alpha|, \end{cases} \quad (26)$$

In the situation of our concern, where $g, \bar{g} \gg \Gamma, \bar{\Gamma}$, the first case is non-resonant, since $G \gg |\alpha|$. On the other hand, the second case may fall in the resonance region. Note that the imaginary part is positive in the second regime unless α is much smaller than γ . In the first regime, on the other hand, the signature of the imaginary part is determined by the competition of the asymmetries in the number densities and the collision rates.

Although we have so far regarded ω as a function of \bar{g} , one can also take other parameters. If one varies g instead of \bar{g} , the same criterion $|A| \approx |\alpha|$ is obtained. This resonance peak, if regarded as a function of one of the collision rates, it reaches the maximum height at a certain value of this rate. Note also that the resonance occurs at $g \sim \bar{g}$ but not exactly at $g = \bar{g}$. To see this more clearly, we choose a different parameter set, in which we artificially raise the collision rate of antineutrinos to an unrealistically high value $\bar{\Gamma} = 0.025 \text{ cm}^{-1}$ so that $|\alpha| \approx 0.025 \text{ cm}^{-1}$. We then obtain $\bar{g} \approx 1.025 \text{ cm}^{-1}$ at the peak. This deviation from $g = 1 \text{ cm}^{-1}$ is confirmed in Fig.1(c). One should also notice that the resonance amplitude is much larger, and the resonance width is also much broader in this extreme case. A similar analysis shows that the resonance occurs also for the isotropy-breaking branch. The peak location is a bit different from that for the isotropy-preserving mode and satisfies $A^2 = (3\alpha)^2$, as demonstrated in Fig.2(c) again for the exaggerated value of $\bar{\Gamma} = 0.025 \text{ cm}^{-1}$. It is also observed that the resonance width for the isotropy-breaking mode is not appreciably different from that for the isotropy-preserving mode whereas the resonance strength is weaker by a factor ~ 2 for the isotropy-breaking mode than that for the isotropy-preserving mode.

So far we have employed the dispersion relation. The behavior discussed above can be also derived directly from the original quantum kinetic equation. Since it provides a different insight into the resonance, we will

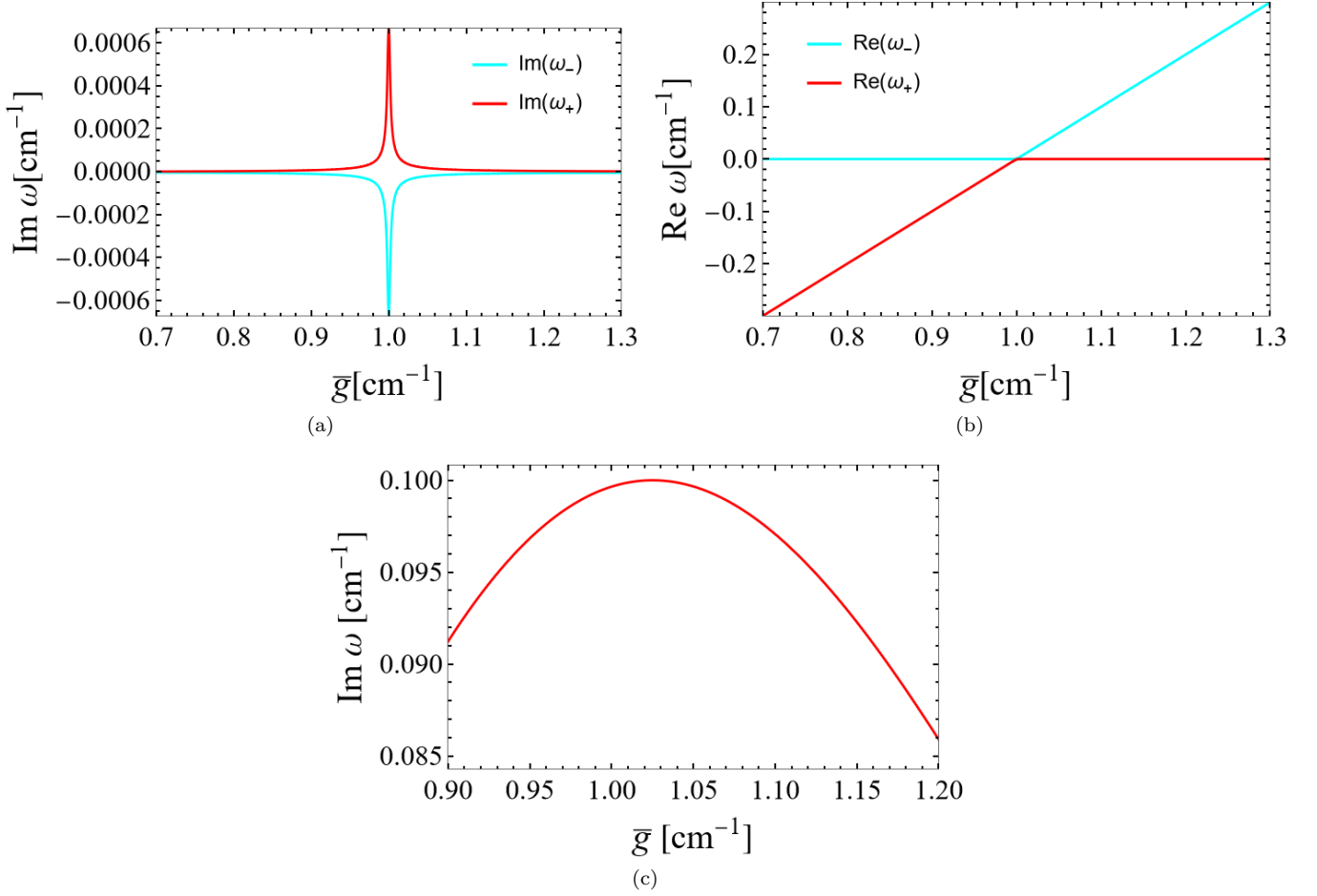


FIG. 1. Real and imaginary parts of the complex frequency ω for the isotropy-preserving branch as a function of \bar{g} . For (a) and (b) we take $g = 1 \text{ cm}^{-1}$, $\gamma = 2.05 \times 10^{-7} \text{ cm}^{-1}$, $\alpha = -4.5 \times 10^{-8} \text{ cm}^{-1}$, whereas for (c) we artificially magnify the collision rate of antineutrinos to $\bar{\Gamma} = 2.5 \times 10^{-2} \text{ cm}^{-1}$, so that $|\alpha| \sim 2.5 \times 10^{-2} \text{ cm}^{-1}$ which implies $\bar{g} \approx 1.025 \text{ cm}^{-1}$ at the resonance peak. See the text for the notational details.

look at it below. We assume that the background is homogeneous, isotropic, and monochromatic. The vacuum and matter terms are ignored to focus on CFI. Then the Hamiltonian and the collision term are given as

$$H = H_\nu = H_d + H_o = \begin{pmatrix} f_{\nu_e} - f_{\bar{\nu}_e} & 0 \\ 0 & f_{\nu_x} - f_{\bar{\nu}_x} \end{pmatrix} + \begin{pmatrix} 0 & S - \bar{S} \\ S^* - \bar{S}^* & 0 \end{pmatrix}, \quad (27)$$

$$C = \begin{pmatrix} \Gamma_e(f_{\nu_e,eq} - f_{\nu_e}) & \frac{\Gamma_e + \Gamma_x}{2}(S_{eq} - S) \\ \frac{\Gamma_e + \Gamma_x}{2}(S_{eq}^* - S^*) & \Gamma_x(f_{\nu_x,eq} - f_{\nu_x}) \end{pmatrix}, \quad (28)$$

$$\bar{C} = \begin{pmatrix} \bar{\Gamma}_e(f_{\bar{\nu}_e,eq} - f_{\bar{\nu}_e}) & \frac{\bar{\Gamma}_e + \bar{\Gamma}_x}{2}(\bar{S}_{eq} - \bar{S}) \\ \frac{\bar{\Gamma}_e + \bar{\Gamma}_x}{2}(\bar{S}_{eq}^* - \bar{S}^*) & \bar{\Gamma}_x(f_{\bar{\nu}_x,eq} - f_{\bar{\nu}_x}) \end{pmatrix}.$$

Note that the Hamiltonian is divided into the diagonal part H_d and the off-diagonal part H_o . The equilibrium

distributions are set to the unperturbed states:

$$\begin{aligned} f_{\nu_i,eq} &= f_{\nu_i}, \\ f_{\bar{\nu}_i,eq} &= f_{\bar{\nu}_i}, \\ \bar{S}_{eq}^{(*)} &= S_{eq}^{(*)} = 0. \end{aligned} \quad (29)$$

The linearized equations for S and \bar{S} are given as

$$i\partial_t \mathbf{V} = \mathbf{W} \mathbf{V}, \quad (30)$$

where \mathbf{V} is vector defined as

$$\mathbf{V} = \begin{pmatrix} S \\ \bar{S} \end{pmatrix}, \quad (31)$$

and \mathbf{W} is the matrix expressed as

$$\begin{pmatrix} -(f_{\bar{\nu}_e} - f_{\bar{\nu}_x}) - i\frac{1}{2}(\Gamma_e + \Gamma_x) & (f_{\nu_e} - f_{\nu_x}) \\ -(f_{\bar{\nu}_e} - f_{\bar{\nu}_x}) & (f_{\nu_e} - f_{\nu_x}) - i\frac{1}{2}(\bar{\Gamma}_e + \bar{\Gamma}_x) \end{pmatrix}. \quad (32)$$

Note that we assume that the perturbation is also isotropic in deriving these equations here.

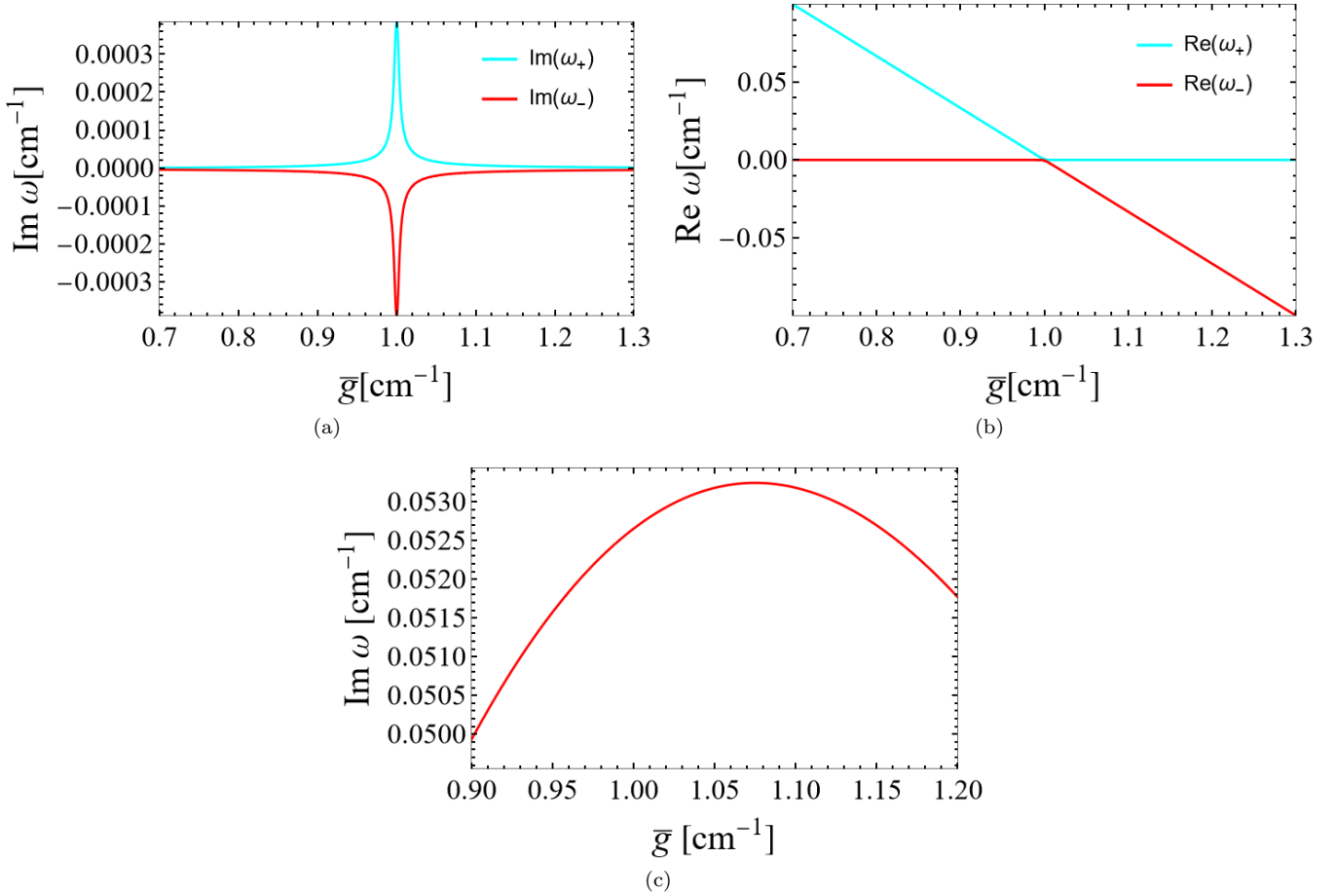


FIG. 2. Same as Fig.1 but for the isotropy-breaking branch.

The general solution is given as the superposition of two independent solutions:

$$\mathbf{V}(t) = \mathbf{V}_+ e^{-i\omega_+ t} + \mathbf{V}_- e^{-i\omega_- t}, \quad (33)$$

where \mathbf{V}_\pm , ω_\pm are the eigenvectors and eigenvalues to the matrix W . The eigenvalues are obtained as [30]

$$\omega_\pm = -A - i\gamma \pm \sqrt{A^2 - \alpha^2 + 2iG\alpha}, \quad (34)$$

where the notations are identical to those for Eq.19.

It is interesting to point out that the elimination of the diagonal part of the Hamiltonian does not change the two eigenvalues, which suggests that CFI is driven by an interplay of the off-diagonal part of the Hamiltonian and the collision terms. That may be illuminated more clearly by treating the collision term as a perturbation. Let us first consider the case with $H = H_0$ and no collision term $C = 0$. The eigenvalues and eigenvectors in this case are given as

$$\begin{aligned} \omega_1 = 0, \quad \mathbf{V}_1 &= \begin{pmatrix} 1 \\ 1 \end{pmatrix}, \\ \omega_2 = -f - \bar{f}, \quad \mathbf{V}_2 &= \begin{pmatrix} f \\ \bar{f} \end{pmatrix}. \end{aligned} \quad (35)$$

where and below we introduce the following notations:

$$\begin{aligned} f &= f_{\nu_e} - f_{\nu_x}, \quad \bar{f} = f_{\bar{\nu}_e} - f_{\bar{\nu}_x}, \\ \Gamma &= \frac{1}{2}(\Gamma_e + \Gamma_x), \quad \bar{\Gamma} = \frac{1}{2}(\bar{\Gamma}_e + \bar{\Gamma}_x), \end{aligned} \quad (36)$$

This is a stable flavor evolution with no growth of amplitudes.

Now we reinstate the collision terms but as a perturbation. The characteristic equation is then written as

$$[-f - (\omega_0 + \Delta\omega) - i\Gamma] [\bar{f} - (\omega_0 + \Delta\omega) - i\bar{\Gamma}] + f\bar{f} = 0, \quad (37)$$

where the eigenvalue is expressed as the sum of the unperturbed value given in Eq.35 and a (small) shift. To the linear order, the shifts are obtained for the two modes as

$$\begin{aligned} \Delta\omega_1 &\approx \frac{if\bar{\Gamma} - i\bar{f}\Gamma}{f - \bar{f}}, \\ \Delta\omega_2 &\approx \frac{if\Gamma - i\bar{f}\bar{\Gamma}}{\bar{f} - f}. \end{aligned} \quad (38)$$

They are divergent at $f = \bar{f}$ unless $\Gamma = \bar{\Gamma}$, which is an indication of the resonance in the current setting,

i.e., the collision term is assumed to be small and so is the shift, the latter of which is no longer correct at the resonance. Note that the two shifts have opposite signatures, in qualitative agreement with the exact solution.

B. Numerical Simulations

Now we go beyond the linear analysis. We solve the quantum kinetic equation

$$i\partial_t\rho = [H_\nu, \rho] + iC \quad (39)$$

for the homogeneous, isotropic, and monochromatic neutrino distributions. The vacuum and matter terms are omitted again. The following simulations are meant to study the nonlinear evolution of the isotropy-preserving mode both in the non-resonance and resonance regions. For this purpose we vary rather arbitrarily f , the distribution function of antineutrino. For comparison, we also run linear simulations, in which the Hamiltonian is fixed to the initial value.

Since the vacuum term, which would produce perturbations to the flavor eigen state automatically, is neglected here, we give an initial perturbation by hand as follows:

$$\begin{aligned} f &= f_{\nu_e} = 1 \text{ cm}^{-1}, \\ \bar{f} &= f_{\bar{\nu}_e} \text{ is a free variable,} \\ S &= \bar{S} = 10^{-8} + 0i \text{ cm}^{-1}. \end{aligned} \quad (40)$$

For simplicity, we assume that all neutrinos are initially in the electron flavor and the initial perturbation is isotropic so that the isotropy-breaking mode does not appear in this simulation. As discussed in the previous section, the occurrence of CFI is dictated by the four quantities: f , \bar{f} , Γ and $\bar{\Gamma}$ (see Eq.36). Note that in the linear simulations, f and \bar{f} are conserved quantities and unchanged in time.

The collision rates are chosen as

$$\begin{aligned} \Gamma_e = \Gamma_x &= \frac{\Gamma}{2} = 1.6 \times 10^{-7} \text{ cm}^{-1}, \\ \bar{\Gamma}_e = \bar{\Gamma}_x &= \frac{\bar{\Gamma}}{2} = 2.5 \times 10^{-7} \text{ cm}^{-1}, \end{aligned} \quad (41)$$

which correspond to

$$\begin{aligned} \gamma &= 2.05 \times 10^{-7} \text{ cm}^{-1}, \\ \alpha &= -4.5 \times 10^{-8} \text{ cm}^{-1}. \end{aligned} \quad (42)$$

Since the Γ and $\bar{\Gamma}$ are much smaller than f and \bar{f} , the resonance peak occurs essentially at $f = \bar{f}$.

The results of the linear simulations are shown first in Fig.3 for three different values of \bar{f} :

1.000 cm⁻¹, 1.009 cm⁻¹ and 1.100 cm⁻¹. The first one almost corresponds to the resonance peak whereas the second and third values give the resonance edge and a non-resonance point, respectively. The blue curves are the modulus of flavor coherence, $|S|$, plotted against time while the yellow lines indicate for comparison the exponential growths with the values of ω_+ given in Eq.19 for these settings. As should be clear, $|S|$ shows the exponential growth as expected in all cases. In particular, the growth is much faster indeed in the resonance. Note also that the initial conditions are not exactly the eigen modes corresponding to ω_+ and some deviations from the exact exponential growth are seen.

Now we proceed to the results of the fully nonlinear simulations run for the first two initial conditions employed in the linear simulations presented just above. They correspond to the resonance peak and edge, respectively. In Fig.4 we plot not only $|S|$, the modulus of the flavor coherence and the off-diagonal component of the density matrix, but also the distribution functions of all neutrinos, which are also the diagonal components of the density matrix, as functions of time. For reference, the exponential growths with the values of ω_+ in Eq.19 for the current settings are again exhibited.

One recognizes clearly that there are two distinct phases, the linear phase, in which the flavor coherence grows exponentially at the rate given in the linear analysis, and the nonlinear saturation phase, where the $|S|$ peaks out and levels off thereafter and the distribution functions of neutrinos and antineutrinos are also settled gradually to steady states that are different from the initial ones. The transition from the linear phase to the nonlinear phase, the decay of f , is triggered by $|S|$. It is found from the result for the resonance that the saturation level of the flavor coherence is not particularly large (actually smaller) compared with the case for the resonance edge and that the role of resonance is just to shorten the time it takes to reach the saturation. This may be supported by another simulation, a variant of the second case, in which the $\bar{\Gamma}$ is changed to $3.6 \times 10^{-7} \text{ cm}^{-1}$ with other parameters, particularly f and \bar{f} , fixed so that it should give the resonance closer to the peak. The result is presented as Fig.4(c). Note that the linear growth rate is twice as large as that in the second case and is close to that in the first case. The saturation occurs earlier consistently with the enhanced linear growth rate. On the other hand, the asymptotic state is almost the same as that in the second case. It is mostly determined by the initial neutrino distributions and little affected by the resonance. What consequences the accelerated saturation may have, if any, for the core-collapse supernova remain to be studied.

It is interesting to point out that in the first case corresponding approximately to the resonance peak, a very fast flavor bouncing occurs in the beginning of the nonlin-

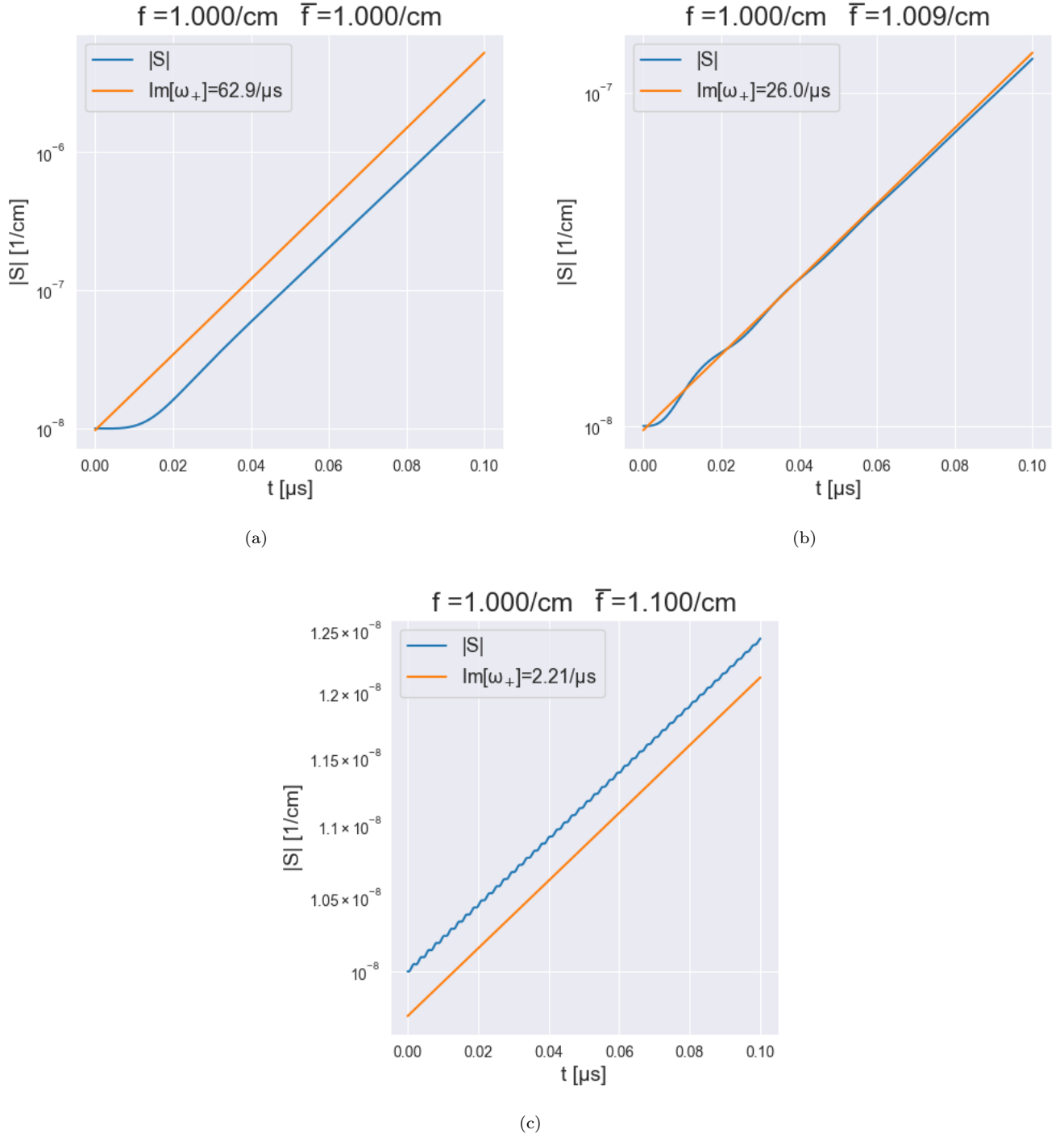


FIG. 3. The time evolutions of $|S|$, the modulus of the flavor coherence, for three values of \bar{f} in the linear simulations. We take $\alpha = -4.5 \times 10^{-8} \text{ cm}^{-1}$ and $f = 1 \text{ cm}^{-1}$. In the plots, the yellow straight lines are the exponential evolution at the growth rate, and the blue curves are numerical. (a) $\bar{f} = 1.000 \text{ cm}^{-1}$ approximately corresponds to the resonance peak, (b) $\bar{f} = 1.009 \text{ cm}^{-1}$ gives a resonance edge, and (c) $\bar{f} = 1.100 \text{ cm}^{-1}$ is in the non-resonance region. As shown in Fig.1(a), (\bar{g} should be identified to the notation \bar{f} used here), the resonance peak is reached at approximately $\bar{f} \approx 1.0 \text{ cm}^{-1}$, the resonance region has a boundary at roughly $\bar{f} \approx (1.0 \pm 0.03) \text{ cm}^{-1}$, and the non-resonance is outside that boundary.

ear saturation phase right after the peak-out. It is due to the diagonal part of the collision term, in which the equilibrium distributions is imposed. In fact, if we reset the equilibrium values to the actual asymptotic values when the nonlinear phase is reached, this feature disappears.

IV. NON-MONOCROMATIC NEUTRINOS

We extend the analyses in the previous section to non-monochromatic neutrinos. We assume that neutrinos and antineutrinos have energy spectra given by the Fermi-Dirac distributions. We begin with the linear analysis and discuss the criterion for the resonance as well as the growth rate at the resonance peak in this case. We then study the nonlinear evolutions of the resonance for the isotropy-preserving mode with $k = 0$ by numerical simulations. Finally, going back to the linear analysis, we investigate the effects of nonvanishing wave numbers in the perturbation as well as anisotropies in the background on CFI. As an extreme case of the latter, we discuss a possible interplay of the resonance in CFI with FFC on the same footing.

A. Linear Analysis

We assume that neutrinos and antineutrinos have continuous energy spectra given by the Fermi-Dirac distributions:

$$f_i(E, g_i, T_i, \mu_i) = \frac{g_i}{\exp[E/T_i - \mu_i] + 1}, \quad (43)$$

where g_i , T_i and μ_i are the model parameters for the neutrino species i , and E is the neutrino energy. Assuming for simplicity that only electron flavor is present initially, we choose

$$\begin{aligned} g_{\nu_e} &= 1, \\ g_{\bar{\nu}_e} &\text{ is a free variable,} \\ g_{\nu_x} &= g_{\bar{\nu}_x} = 0, \end{aligned} \quad (44)$$

and the shorthand notation

$$\begin{aligned} g &= g_{\nu_e}, \\ \bar{g} &= g_{\bar{\nu}_e} \end{aligned} \quad (45)$$

will be used in the following; the temperatures are set to

$$\begin{aligned} T_{\nu_e} &= 4 \text{ MeV,} \\ T_{\bar{\nu}_e} &= 5 \text{ MeV;} \end{aligned} \quad (46)$$

we further assume that $\mu = 0$. Although it is not presented here, we confirmed that a non-zero μ does not change qualitatively the result in the following. The collision term is now assumed to depend on the energy quadratically as

$$\Gamma(E) = \Gamma_0 \left(\frac{E}{10 \text{ MeV}} \right)^2, \quad (47)$$

with

$$\Gamma_0 = 10^{-5} \text{ cm}^{-1} \quad (48)$$

common to all flavors.

For later convenience we introduce the number density n_i , the mean energy $\langle E \rangle_i$, and the mean collision rate $\langle \Gamma \rangle_i$ for the neutrino species i as

$$\begin{aligned} n_i &= \frac{1}{(\hbar c)^3} \int \frac{E^2 dE}{2\pi^2} f(E, g_i, T_i, \mu_i), \\ \langle E \rangle_i &= \frac{1}{n_i} \int \frac{E^3 dE}{2\pi^2} f(E, g_i, T_i, \mu_i), \\ \langle \Gamma \rangle_i &= \frac{1}{n_i} \int \frac{E^2 dE}{2\pi^2} \Gamma(E) f(E, g_i, T_i, \mu_i). \end{aligned} \quad (49)$$

Note that a change in g_i influences only the number density n_i while a variation in T_i or μ_i influences all of n_i , $\langle E \rangle_i$, $\langle \Gamma \rangle_i$.

We solve Eq.15 numerically to obtain the dispersion relation. In doing so, the energy range from 0 MeV to 80 MeV is divided into nonuniform 128 bins concentrated more at low energies.

We plot in Fig.5 the contour lines for $\text{Re } I = -1$ or 3 (blue) and $\text{Im } I = 0$ (orange) in the complex ω plane for some representative values of \bar{g} . The intersection of the two contour lines gives the dispersion relation $\omega(k)$ at $k = 0$. One of the two solutions (except for the origin) with a positive imaginary part is the unstable mode. The first three plots in the figure are for the isotropy-preserving branch at $\bar{g} = 0.51, 0.511, 0.512$, respectively, and the last plot is for the isotropy-breaking branch at $\bar{g} = 0.512$. For the current choice of parameters, which correspond to

$$\begin{aligned} \langle \Gamma \rangle &= 2.07031 \times 10^{-6} \text{ cm}^{-1}, \\ \langle \bar{\Gamma} \rangle &= 3.23531 \times 10^{-6} \text{ cm}^{-1}, \\ \alpha &= \frac{\langle \Gamma \rangle - \langle \bar{\Gamma} \rangle}{2} \approx -5.825 \times 10^{-7} \text{ cm}^{-1}, \end{aligned} \quad (50)$$

the resonance peak is expected to occur approximately at $\bar{g} = 0.512$ (panels (c) and (d)) giving $n \approx \bar{n} \approx 4.88691 \text{ cm}^{-1}$. This is confirmed in Fig.6, where we plot the real and imaginary parts of ω for the unstable isotropy-preserving branch as a function of \bar{g} . One can see a familiar enhancement of the imaginary part, or the growth rate of the instability.

We also investigate an extreme case, in which we artificially magnify the collision rate $\bar{\Gamma}$ of antineutrino by five orders of magnitude, $\Gamma_0 = 1 \text{ cm}^{-1}$ in Eq.48, while other parameters are unchanged. This gives $\alpha = -1.6174 \text{ cm}^{-1}$. The result is shown in Fig.6(c). The resonance peak occurs at $\bar{g} = 0.74$, which corresponds to $A = -1.0081 \text{ cm}^{-1}$. The number density of antineutrino

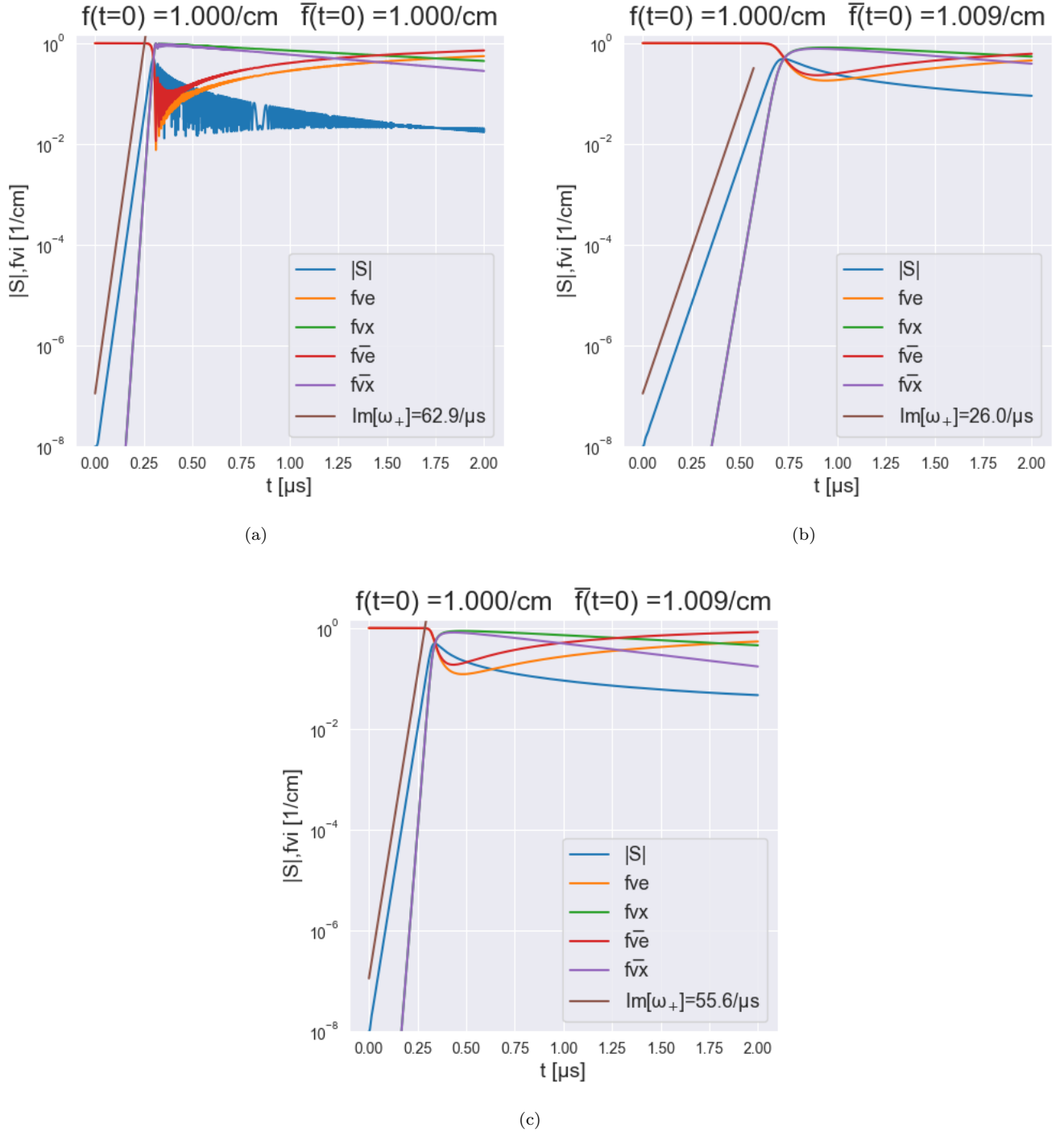


FIG. 4. (a) and (b): the nonlinear time evolutions for the same initial conditions as in Figs.3(a) and 3(b), respectively. Not only the flavor coherence $|S|$ (blue lines) but also the distribution functions of neutrinos and antineutrinos (colors indicated in the legends) are presented. (c): a variant of (b), in which $\bar{\Gamma}$ is changed to $3.6 \times 10^{-7} \text{ cm}^{-1}$ so that the initial condition should be closer to the resonance peak.

is noticeably different from that of neutrino in this case just as inferred from the result of the monochromatic case. Again the approximate formula (orange line) is compared with the numerical result shown in blue.

This time the approximation is not so successful as before although the peak shift as well as the broadening of resonance are captured qualitatively. It is pointed out that thanks to this broadening the case with the

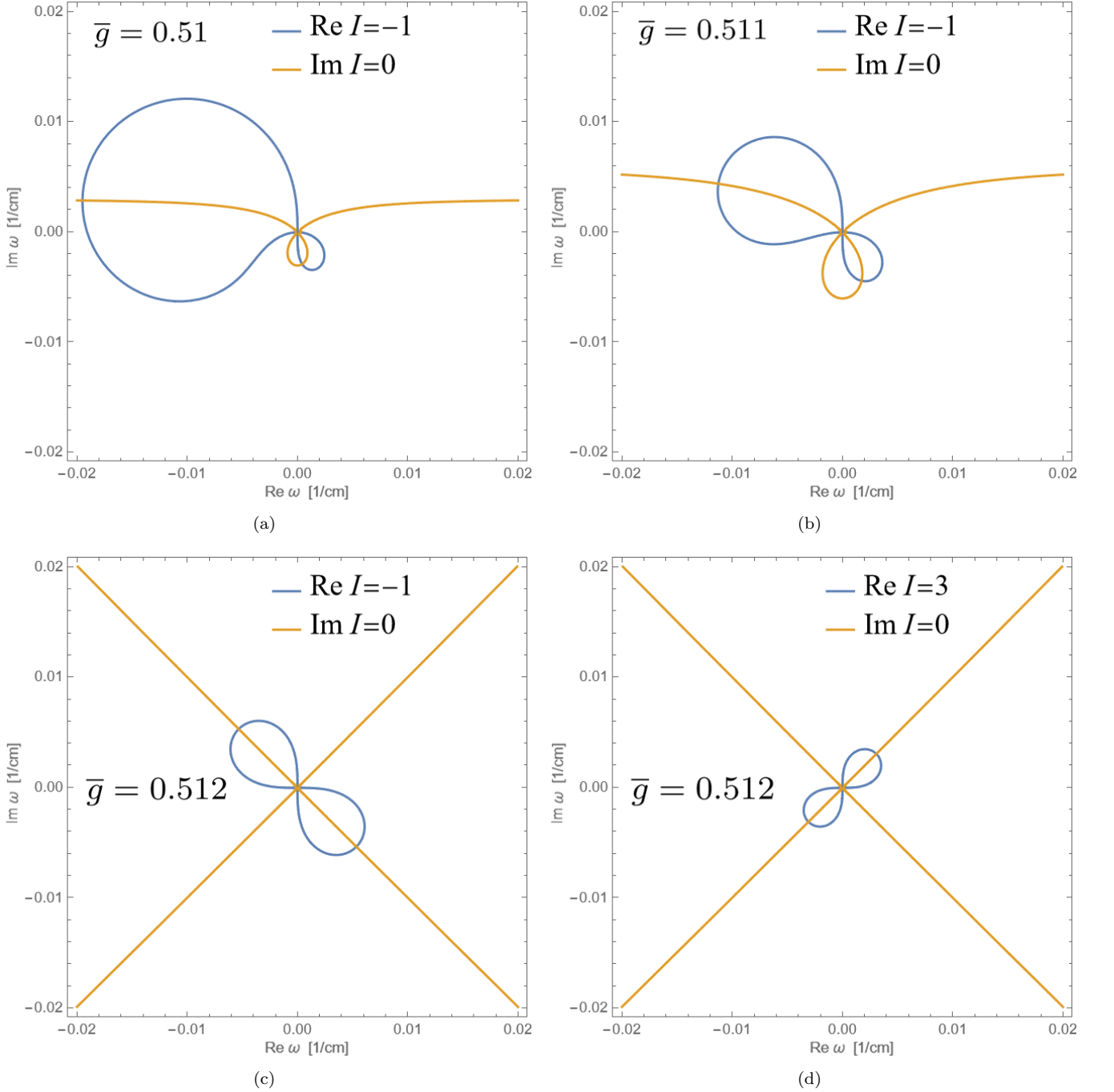


FIG. 5. The contours lines for $\text{Re } I = -1$ or 3 (blue) and $\text{Im } I = 0$ (orange) in Eq.15. Their intersections give the dispersion relation $\omega(k=0)$. Panels (a)-(c) are for the isotropy-preserving branch whereas panel (d) displays the result for the isotropy-breaking branch.

equal number densities, $n = \bar{n}$, is still in the resonance, although not at the peak, and hence the growth rate is enhanced. We explored other neutrino spectra, such as the Fermi-Dirac distributions with non-vanishing chemical potentials or the Gaussian and polynomial distributions that are not too irregular. The results are qualitatively the same as those given above and hence

will not be presented here.

Finally, it is worth pointing out that the growth rate around the resonance is well approximated by the formula for the monochromatic case, Eq.19 for ω_+ , with

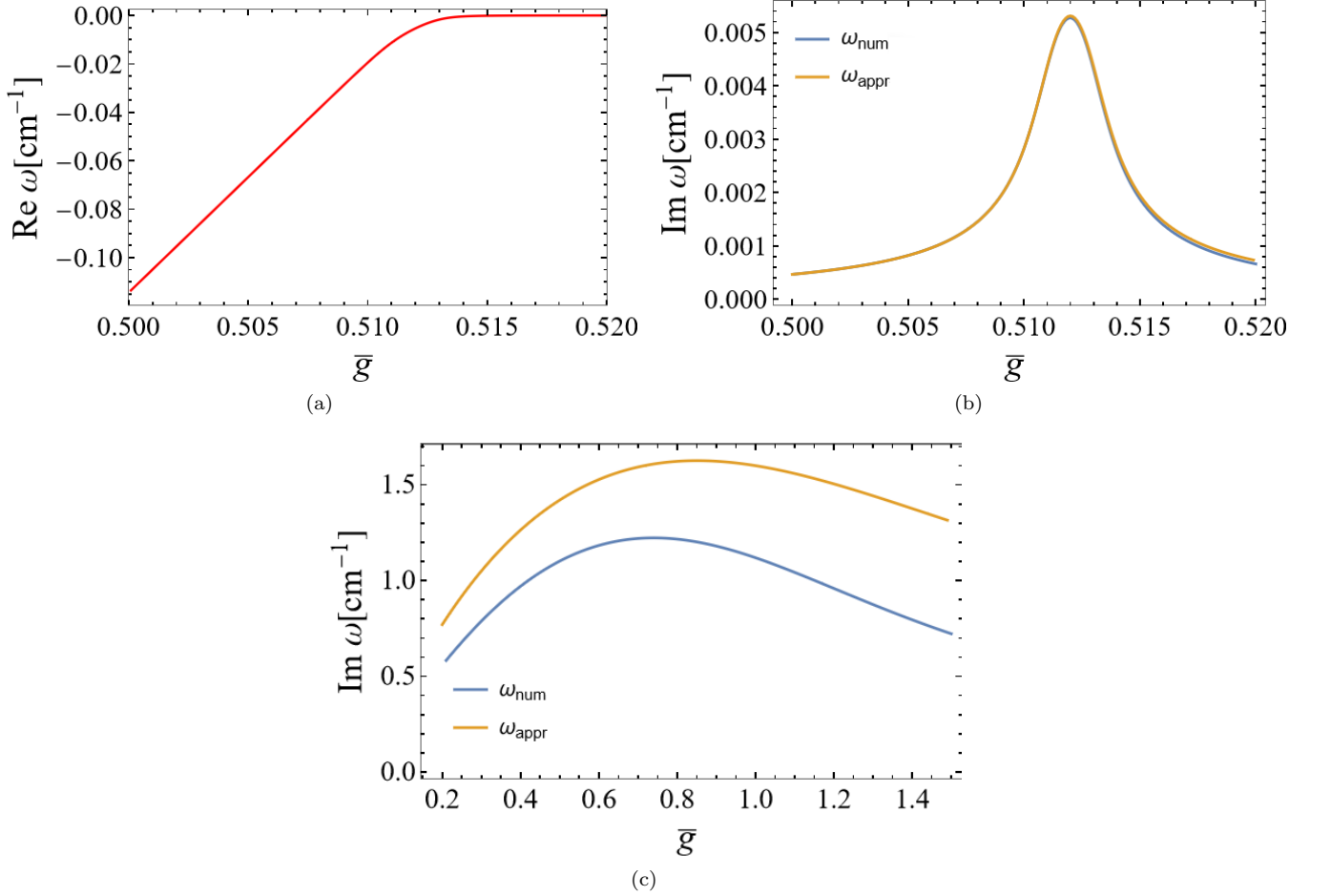


FIG. 6. The real (a) and imaginary (b) parts of the complex frequency ω for the unstable isotropy-preserving branch as a function of \bar{g} . For the imaginary part, the numerical solution $\text{Im } \omega_{\text{num}}(\bar{g})$ shown in blue is compared with the approximate one $\text{Im } \omega_{\text{appr}}(\bar{g})$ exhibited in orange. In panel (c), the collision rate $\bar{\Gamma}$ of antineutrinos is artificially magnified by 10^5 .

the following substitutions:

$$\begin{aligned}
 g &\rightarrow n, \\
 \bar{g} &\rightarrow \bar{n}, \\
 \Gamma &\rightarrow \langle \Gamma \rangle, \\
 \bar{\Gamma} &\rightarrow \langle \bar{\Gamma} \rangle.
 \end{aligned}
 \tag{51}$$

Note that this approximate formula agrees with the one derived previously in [33] under the assumption of $|\Gamma|, |\bar{\Gamma}| \ll |\omega|$ if γ and α^2 are neglected accordingly. This is demonstrated in Fig.6(b), where the numerical solution displayed in blue is compared with the approximate one presented in orange. Their agreement matches what was shown in [33]. Although the criterion for resonance posited in that paper is appropriate only when the collision rates are small, the condition $|A| \sim |\alpha|$ is always satisfied at the resonance regardless of the parameter values.

B. Numerical Simulations

We again solve Eq.39 numerically for homogeneous and isotropic neutrinos with the Fermi-Dirac distributions as the energy spectra. The background distributions are actually the same as those employed for the linear analysis in the previous section, Eqs.44-48. Since the vacuum term is omitted in the kinetic equation, we need to set an initial perturbation by hand, which is also assumed to be isotropic and homogeneous. Hence only the isotropy-preserving branch is considered. We take \bar{g} as a free parameter and vary it so that the unperturbed state is either near the resonance peak or near the resonance edge.

In the simulation, the energy range from 1 MeV to 100 MeV is divided uniformly into 100 bins this time. We adopt the following initial perturbations only to the

off-diagonal components of the density matrix

$$\begin{aligned} S(E) &= (1 + 0.8i)10^{-5}f(E), \\ \bar{S}(E) &= (-0.5 + i)10^{-5}\bar{f}(E). \end{aligned} \quad (52)$$

The numbers in the functions are chosen rather arbitrarily.

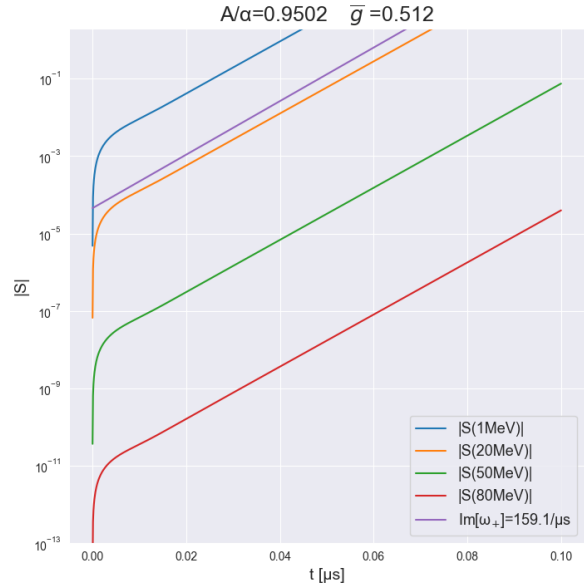
The results of the linear simulations, in which the Hamiltonian is fixed to the initial value, is shown in Fig.7 for two choices of \bar{g} , one corresponding approximately to the resonance peak and the other giving the resonance edge. The value of A/α measures how close the initial configuration is to the resonance peak: the closer to unity it is, the nearer to the resonance peak the initial state is. It is evident that the flavor coherence grows at a common rate for all energies[30], just as expected from the energy-independent nature of $\omega(k)$. In the resonance, it grows much faster indeed.

The corresponding results for the nonlinear simulations are presented in Fig.8. Again one recognizes that the linear phase is followed by the nonlinear saturation phase also in this case with the non-monochromatic energy spectra. In the linear phase the flavor coherence grows at a common rate for all energies just as in the linear simulations given above. In the resonance case (panel (a)), the nonlinear phase is reached much faster than in the non-resonance case (panel (b)).

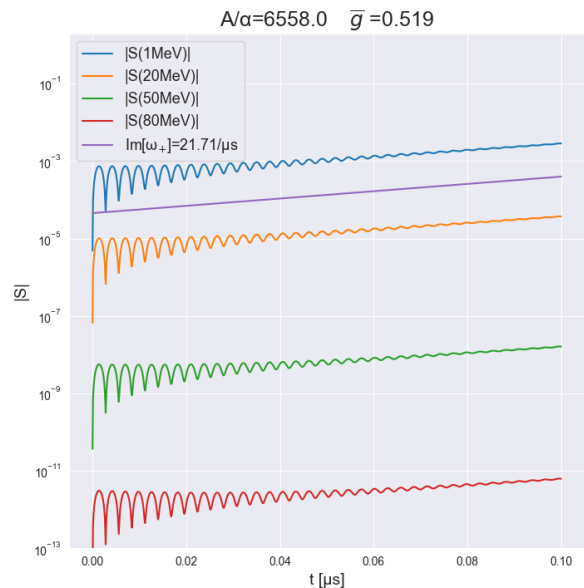
It is also found that the beginning of the nonlinear phase is marked for each energy when $|S(E)| = f(E)$ is satisfied individually, which is a direct extension of the monochromatic case. The saturation level is not much different between the resonance and non-resonance cases, indicating again that the main effect of resonance is to accelerate the linear growth and the asymptotic state is hardly affected by the resonance. The bouncing in the nonlinear phase is observed only for the resonance case. The bouncing amplitude seems to be related with the difference between the equilibrium distribution and the asymptotic distribution although the exact mechanism of bouncing is not clear at the moment. This is induced by the diagonal part of the collision term. In fact, if we discard the diagonal part effectively by resetting the equilibrium distributions to the asymptotic ones, the bouncing feature is gone just as in the monochromatic case.

C. $k \neq 0$ Perturbation/Anisotropy in Background

In this last section, we investigate the resonance either for $k \neq 0$ perturbations in the homogeneous and isotropic background or for $k = 0$ modes in the homogeneous but anisotropic background. We work on the dispersion relations in the linear regime. The neutrino energy spectra are again assumed to be the



(a)



(b)

FIG. 7. The time evolutions of $|S|$, the modulus of the flavor coherence, at different neutrino energies in the linear simulations for the continuous energy spectrum. Two values of \bar{g} are adopted: $\bar{g} = 0.512$ and 0.519 ; $\alpha = -1.165 \times 10^{-6} \text{ cm}^{-1}$, and $g = 1$ giving $n_{\nu_e} = 7.609 \times 10^{32} \text{ cm}^{-3}$. The violet lines indicate for reference the exponential evolution at the growth rate given by the linear analysis.

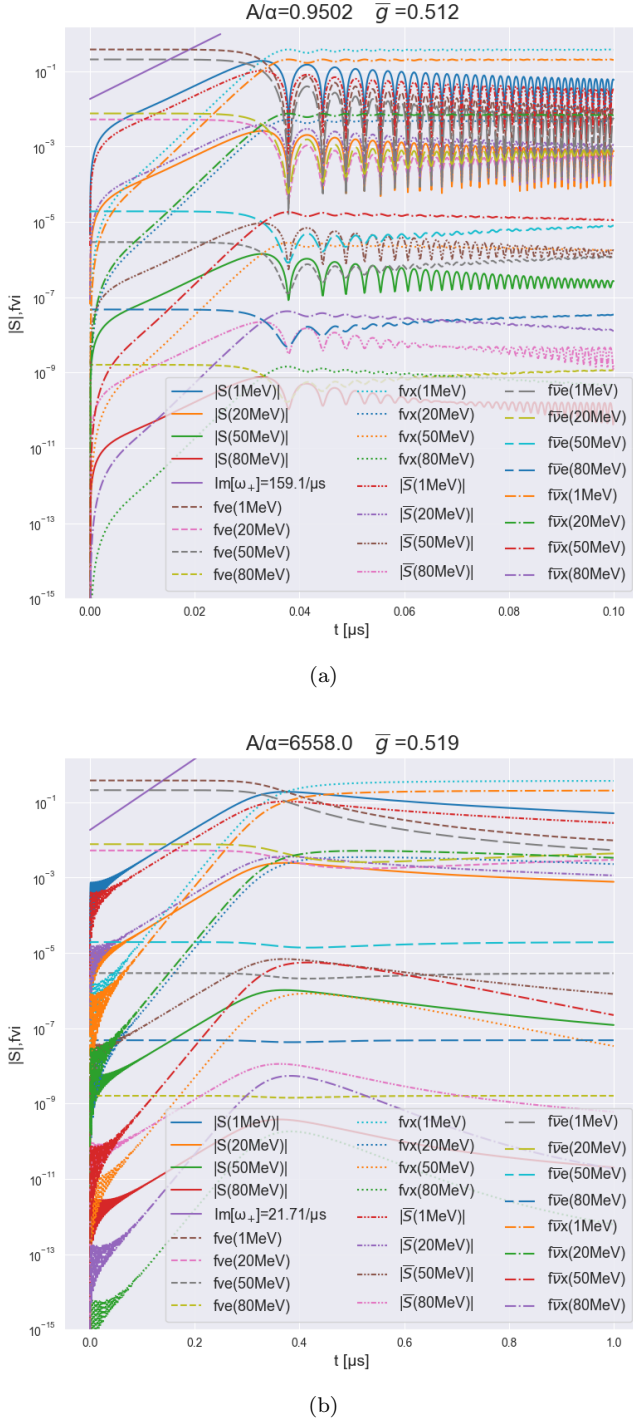


FIG. 8. The nonlinear time evolutions for the same initial conditions as in Fig.7. Not only the flavor coherence $|S|$ but also the distribution functions of neutrinos and antineutrinos are presented for different energies (linetypes given in the legend). The purple solid line indicates the exponential growth at the rate given by the linear analysis.

Fermi-Dirac distributions given in Eq.43, with the same parameters as in Eqs.44-46 and, in addition, with $\bar{g} = g_{\bar{\nu}_e} = 0.512$, corresponding to the resonance peak at $k = 0$. The collision rates are given by Eqs.47-48.

We begin with the $k \neq 0$ perturbation in the homogeneous and isotropic background. In the following the wave vector \mathbf{k} is assumed to be parallel to the z-axis. We solve Eq.14 numerically to obtain the dispersion relation. For $k \neq 0$, there appear two nonvanishing off-diagonal components in Π_{ex} in addition to the diagonal ones, which survive in the $k \rightarrow 0$ limit. In order to see how the isotropy-preserving and isotropy-breaking branches at $k = 0$ are mixed with each other to new modes in the $k \neq 0$ case, we decompose Π_{ex} as

$$\Pi_{ex}^{\mu\nu} = \eta^{\mu\nu} + A^{\mu\nu}. \quad (53)$$

Then its determinant can be written explicitly in a simple form as

$$\det \Pi_{ex} = (A^{11} - 1)^2 [(A^{00} + 1)(A^{33} - 1) - (A^{03})^2], \quad (54)$$

where the following relations

$$\begin{aligned} A^{11} &= A^{22}, \\ A^{30} &= A^{03}, \end{aligned} \quad (55)$$

are used. Note that in the limit of $k = 0$, the following relations hold further:

$$\begin{aligned} A^{30} &= A^{03} = 0, \\ A^{33} &= A^{11} = A^{22}, \end{aligned} \quad (56)$$

and the dispersion relation is obtained from

$$\det \Pi_{ex} = (A^{00} + 1)(A^{11} - 1)^3 = 0. \quad (57)$$

In fact, the isotropy-preserving branch is derived from the first factor and the isotropy-breaking branch is originated from the second factor. In the case of $k \neq 0$, while $A^{11} - 1 = 0$ is unchanged, $(A^{00} + 1)(A^{11} - 1) - (A^{03})^2 = 0$ now mixes the isotropy-preserving and isotropy-breaking branches to produce four branches in general. In the following we look into these modes in detail.

From the first factor in Eq.54, a pair of solutions are obtained, which take the following form $a = (0, a_x, a_y, 0)$, which is perpendicular to \mathbf{k} , and hence break the isotropy in the $x - y$ plane. On the other hand, the second factor can vanish in three different manners: (1) $A^{00} + 1 = A^{03} = 0$, (2) $A^{33} - 1 = A^{03} = 0$, or (3) $(A^{00} + 1)(A^{33} - 1) = (A^{03})^2 \neq 0$. The first case produces a solution of the form: $a = (a_t, 0, 0, 0)$, which is isotropy-preserving. The second case leads to $a = (0, 0, 0, a_z)$, which is hence isotropy-breaking in the z direction, that is, the direction of \mathbf{k} . The last one yields a solution with the form of $a = (a_t, 0, 0, a_z)$ in general, which is also isotropy-breaking. If the first factor and

second factors vanish simultaneously, the solution takes a combined form: for example, the combination of the first factor with case (1) for the second factor has a solution of the following form: $a = (a_t, a_x, a_y, 0)$. these cases are exceptional, though, and occur only for special spectra/collision rates. In fact, we find that case (3) is always satisfied in the second factor of Eq.54 for the ranges of k and \bar{g} considered in this paper.

In Fig.9, we display plots of the contours indicated in each panel for $k = 0.001 \text{ cm}^{-1}$. The left panel gives the solutions for the first factor in Eq.54 whereas the right panel shows the solutions for the second factor. The latter corresponds to case (3) as mentioned above. At this small k , all the modes are not much different from the counterparts at $k = 0$. For later convenience, we refer to the solutions for unstable modes in these plots as Q, W, and Y. Mode Q originated from the first factor in Eq.54 merges at $k = 0$ with Y from the second factor to give the isotropy-breaking modes. On the other hand, mode W is reduced to the isotropy-preserving mode at $k = 0$. These modes are all isotropy-breaking at $k \neq 0$. In Fig.10 we plot the linear growth rates, $\text{Im}\omega$, for these three modes as a function of \bar{g} at the same value of $k = 0.001 \text{ cm}^{-1}$. The resonance feature is evident in all cases around $\bar{g} = 0.512$.

In Fig.11, we show the k -dependence of these growth rates at $\bar{g} = 0.512$, i.e., around the resonance peak. It is apparent that they decrease monotonically with k , indicating that the resonance is suppressed by the non-vanishing k for all modes. This is actually true in the non-resonance region as well. The non-zero k tends to suppress the CFI itself. It is noted that the presence of \mathbf{k} in the denominator of Eq.14 poses a challenge in the numerical integration by discretization in the region $-k < \text{Re}\omega < k$, $0 < \text{Im}\omega < \Gamma(E_{max})$. We do not think that the numerical solutions in these ranges are reliable and hence do not consider those solutions out of resonance or at resonance but suppressed by large values of k , which tend to this region.

Next we study the effect of the anisotropy in the homogeneous neutrino background on the resonance. We introduce the following angular-dependence to the neutrino distributions in momentum space:

$$f_i(E, g_i, T_i, \mu_i, \theta, \delta_i) = (1 + \delta_i \cos\theta) f_i(E, g_i, T_i, \mu_i), \quad (58)$$

where $f_i(E, g_i, T_i, \mu_i)$ on the right hand side is the Fermi-Dirac distribution for neutrino species i ; $0 < \theta < \pi$ is the angle that the neutrino velocity makes with the radially outward direction; the factor δ_i controls the degree of anisotropy. Since we are interested in the resonance in CFI in this paper, we first consider a case with no angular crossing, and hence no FFC. We then look at two cases with different angular crossings to see the interplay between the resonance in CFI and FFC. We solve Eq.14 numerically for $k = 0$ to obtain the

dispersion relation $\omega(k = 0)$ for the anisotropic (but homogeneous) background just described. Note that the integration over the solid angle can be done analytically for $k = 0$.

We first present the results for the first case, in which only electron-type neutrinos and antineutrinos are present initially with the same anisotropy: $\delta = \bar{\delta}$. We choose the model parameters as in Eqs.44-48 together with $\bar{g} = 0.512$ and $k = 0$ so that the unperturbed state corresponds to the resonance peak at $\delta = 0$. We vary the value of δ to see how the anisotropy affects CFI in the resonance. The choice of $k = 0$ simplifies the analysis a lot. In fact, only Π_{ex}^{03} , which is linear in δ , is non-vanishing as the off-diagonal components of Π_{ex} just as in the previous case with $k \neq 0$, and the diagonal components are unchanged from those for the isotropic case. Since the dispersion relation is obtained from $\det \Pi_{ex}$ given as Eq.54 again, we refer to the corresponding modes as Q, W, and Y. Under the current setting, all modes are isotropy-breaking for $\delta \neq 0$. Note that mode Q is independent of δ and $\bar{\delta}$ in this setting, and is always identical to the isotropy-breaking mode for isotropic neutrinos.

In Fig.12 we plot the linear growth rates for the three modes Q, W and Y as functions of \bar{g} at $\delta = 0.4$ to show that the resonance occurs indeed also in this case. Note that Q and Y are strictly distinct from each other at $\delta \neq 0$. In Fig.13 we demonstrate how the background anisotropy affects CFI. It is observed that it tends to suppress CFI. This time the effect is pretty minor, though.

Now we go on to the study of a possible interplay of the resonance in CFI with FFC. For this purpose we choose

$$\begin{aligned} \delta &= 0.1, \\ \bar{\delta} &= 0.08. \end{aligned} \quad (59)$$

The values of other model parameters are unchanged from the previous case for $\delta = \bar{\delta}$. We adjust \bar{g} so that there should be an ELN crossing in the angular distributions of ν_e and $\bar{\nu}_e$. There is indeed an interval of \bar{g} , in which the angular ELN crossing and thus FFC occur. In this model, ν_e is dominant in the radially outward direction while the opposite is true in the inward direction. Note that the mean energies and collision rates for $\bar{\nu}$ are unchanged by the variation of \bar{g} . We study at $k = 0$ the behavior of the fast-unstable branch in the presence of the collision term.

We show in Fig.14(a) the growth rates of this mode as functions of \bar{g} both with (red) and without (blue) the collision term. As is evident from the latter, FFC occurs in this mode for $0.505 \lesssim \bar{g} \lesssim 0.517$, where $\text{Im}\omega$ is positive. Interestingly, the resonance in CFI takes place almost in the same region as could be inferred from the red line, in which the foot of the resonance peak can be

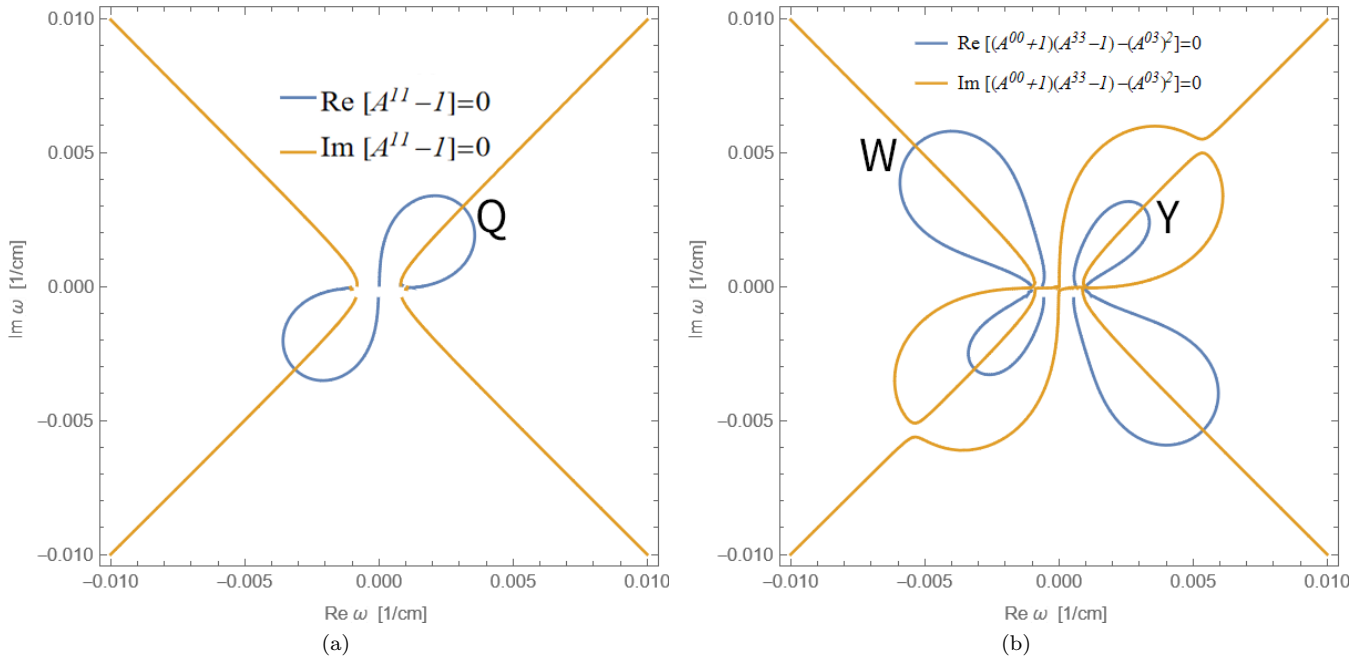


FIG. 9. The plots of the contour lines denoted in each panel in the complex ω plane at $k = 0.001 \text{ cm}^{-1}$.

recognized near the both ends of the FFC range. It is also apparent that the resonance has a very small impact on the growth rate when the FFC is in operation: it only modifies the amplitude very slightly and shifts the peak position only a bit.

This is more evident when we take a different parameter set: $\delta = 0.1$ and $\bar{\delta} = 0.095$. The result is shown in Fig.14(b). In this case, the degrees of anisotropy are not much different between ν_e and $\bar{\nu}_e$ and, as a consequence, the range for the ELN crossing is much narrower in \bar{g} (see the blue line). Now the shift in the peak position by the collisional resonance is apparent. Note that without FFC the resonance height and width are essentially unchanged with this variation of $\bar{\delta}$. Because of this shift, the amplitude of FFC, on the other hand, is enhanced or suppressed, depending on where we look at. Such a shift becomes also noticeable for larger deviations of $\bar{\delta}$ from δ if the difference in the collision rates is large enough. As mentioned above, it seems that when FFC and the resonance in CFI are simultaneously in operation, the growth rate is set by the former (recall that the growth rate of CFI at the resonance peak for the current setting at $\delta = \bar{\delta}$ is $\sim 0.005 \text{ cm}^{-1}$, i.e., 10 times smaller than the growth rate of FFI alone). More systematic investigations in a broader parameter range are certainly needed but will be deferred to future studies.

V. CONCLUSION

We have presented in this paper the results of a systematic study on the resonance of CFI. Employing the two-flavor approximation for simplicity, we have done both linear analysis and nonlinear numerical simulations. The collision is taken into account in the relaxation approximation, which is actually exact for the emission/absorption as well as iso-energetic scatterings of neutrinos. We have always assumed that the neutrino distributions are homogeneous initially but have considered both isotropic and anisotropic distributions in momentum space. We have also taken into account the continuous energy distributions of neutrinos. By changing rather arbitrarily the number densities or the collision rates for the antineutrinos, we have produced both resonance and non-resonance configurations freely.

Starting with the linear analysis of the simplest case, i.e., the monochromatic, homogeneous and isotropic background with $k = 0$ perturbations, we have analytically obtained the dispersion relations both for the isotropy-preserving and isotropy-breaking modes. Note that the latter has been overlooked in the literature so far. We have confirmed that the resonance feature shows up at $A \sim \alpha$ (see Eq.21 for notations) for the isotropy-preserving branch, where the two modes, ω_+ and ω_- (Eq.19), come close to each other. We have demonstrated that a similar feature occurs at $A \sim 3\alpha$ also for the isotropy-breaking branch. In both cases, the resonance peak obtains at $g \sim \bar{g}$ (Eq.17) but not exactly at $g = \bar{g}$. In fact, the deviation becomes larger

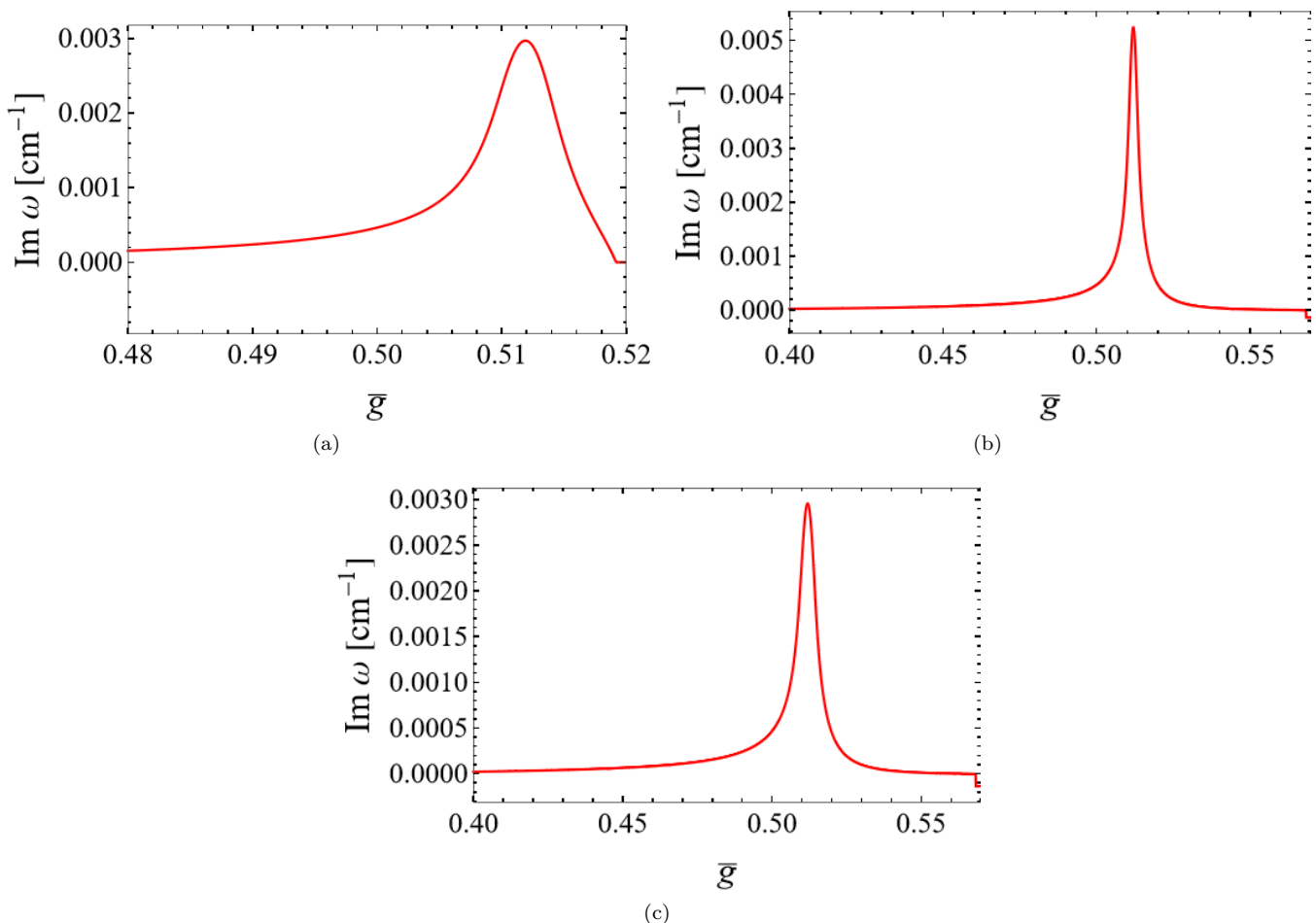


FIG. 10. The resonance features for the unstable branches Q in (a), W in (b), and Y in (c) at $k = 0.001 \text{ cm}^{-1}$.

for a greater difference between the collision rates, Γ for neutrino and $\bar{\Gamma}$ for antineutrinos. The resonance is also broadened in that case.

We have then conducted numerical simulations for the same background setting to investigate the nonlinear evolutions of the perturbations, which were again assumed to have $k = 0$ and added only to the off-diagonal components of the density matrix. We have confirmed the exponential growth at the rate given by the linear analysis in the linear phase, which we have found is followed by the nonlinear saturation phase, where the flavor coherence levels off and the distribution functions are settled to new steady states asymptotically. We have observed a bouncing with large amplitudes only in the resonance case. Its mechanism is unclear for the moment but we have demonstrated that it is induced mainly by the diagonal part of the collision term.

We have then proceeded to the non-monochromatic case, in which we assumed that neutrinos have Fermi-Dirac distributions as their energy spectra. In the linear analysis for the homogeneous and isotropic background

with the $k = 0$ perturbation, we have shown that there are again isotropy-preserving and isotropy-breaking branches and that both of them give resonance. We have also demonstrated that the growth rate around the resonance is well approximated by the exact formula for the monochromatic case with an appropriate substitution of variables as long as the collision rates are not much different between the neutrino and antineutrino. This was pointed out in the previous work [33] for small collision rates. Our results have extended its validity.

The nonlinear simulations have been done for the same background as for the linear analysis above. The perturbation was assumed to have $k = 0$ and to be also isotropic. Only the isotropy-preserving mode has been hence calculated. As expected from the dispersion relation, we have observed that the perturbation grows exponentially at the same rate for all energies of neutrinos. We have found that for different energies of neutrinos the nonlinear saturation phase begins when their flavor coherence becomes of the same amplitude as the distribution functions at their energies, $|S(E)| \sim f(E)$ (Eq.1), a direct extension

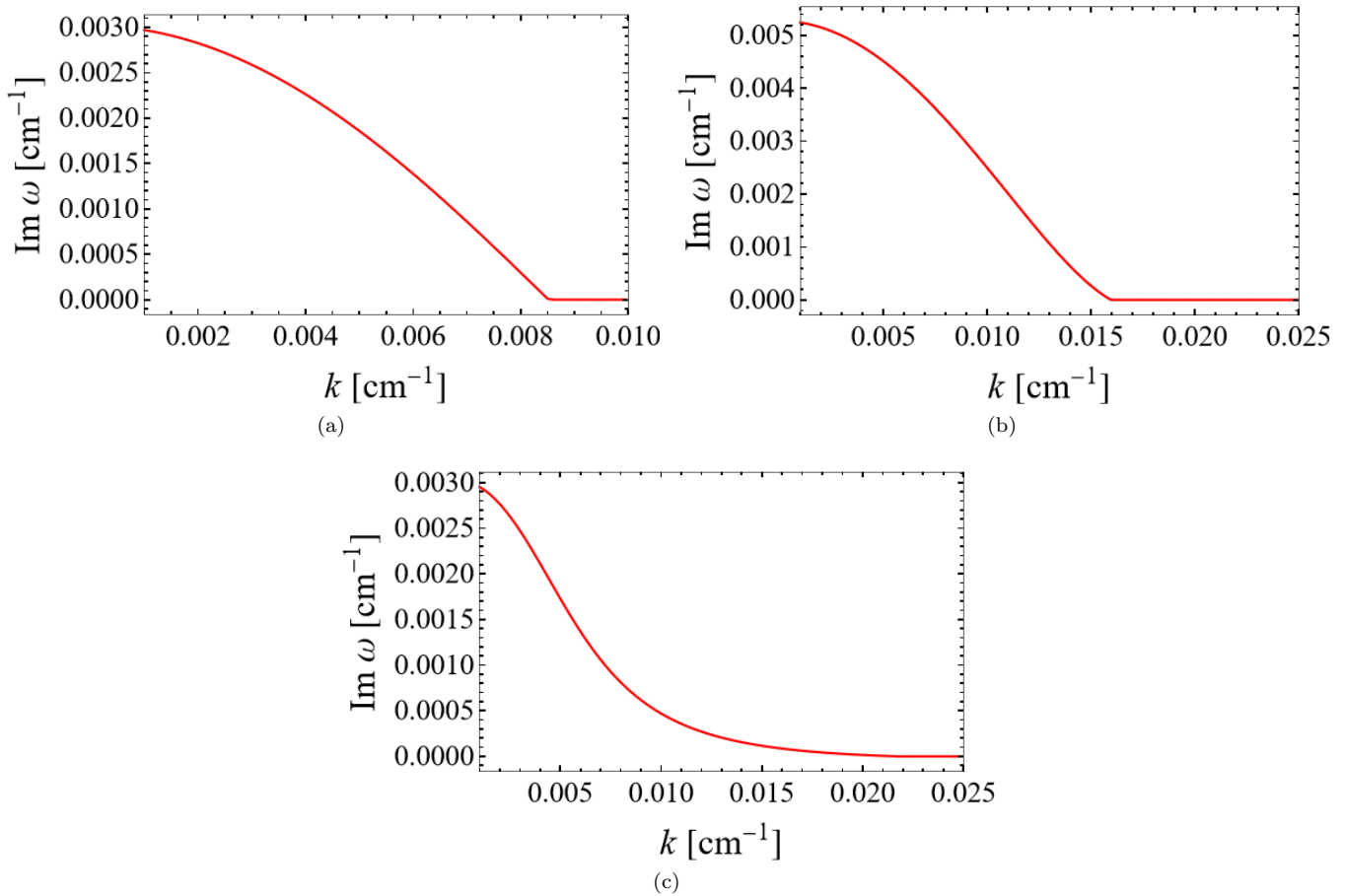


FIG. 11. The linear growth rates for the unstable branches Q in (a), W in (b), and Y in (c) as functions of the wave number k .

of the monochromatic case. We have found that the saturation level is not much affected by the resonance and its main role is to shorten the time it takes to get to the saturation. We have also seen the bouncing of the flavor coherence after its peak-out in the resonance case alone again.

We finally conducted the linear analysis either for the $k \neq 0$ perturbation to the isotropic background or for the $k = 0$ perturbation to anisotropic background configurations. In the former we have shown how the isotropy-preserving and isotropy-breaking branches at $k = 0$ are mixed for $k \neq 0$ to produce new branches and demonstrated that resonance occurs just in the same way for all these modes. We have also found that the non-vanishing k tends to suppress CFI in general.

For the anisotropic background with no electron-lepton-number, or ELN, crossings, we have shown that resonance shows up again in the same way and that the anisotropy tends to suppress CFI, albeit weakly. For the anisotropic background with an ELN crossing, on the other hand, the growth rate is set by the fast flavor conversion, or FFC, and the resonance in CFI, the

region of which tends to overlap with the range of FFC, tends to shift the peak position and broaden the range of instability. The growth rate may be enhanced or suppressed, depending on the position in the unstable range.

There remain many issues to be addressed further. Not to mention, we need to extend the analysis to three flavors. The relaxation approximation should be removed to incorporate non-isoenergetic collisions. The parameter regions considered in this paper are rather limited. For instance, we have investigated rather small k in the $k \neq 0$ perturbation although new modes with different properties may emerge for larger k . Interplays of the resonance in CFI with FFC in the nonlinear phase should be studied, probably numerically. Indeed the growth of the isotropy-breaking modes may induce FFC in that phase. The mechanism of the large-amplitude bouncing in the resonance case needs to be understood. The asymptotic state in the nonlinear saturation phase should be characterized. Eventually we are interested in what consequences, if any, the resonance in CFI may have for core-collapse supernovae and compact object mergers. They will be all future works.

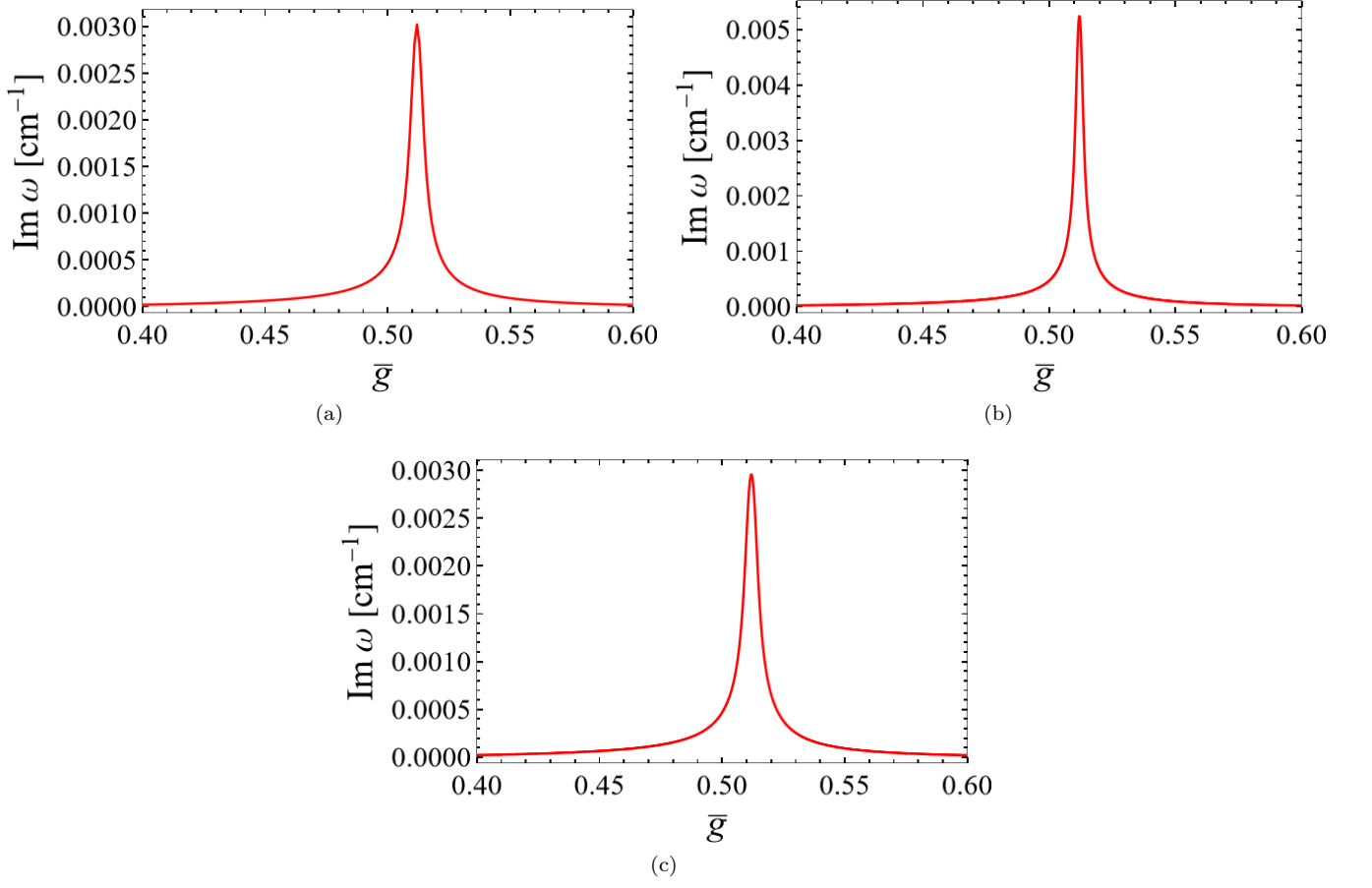


FIG. 12. The resonance features for the anisotropic neutrino backgrounds. The degree of anisotropy is identical for ν_e and $\bar{\nu}_e$: $\delta = \bar{\delta} = 0.4$. (a)-(c) correspond to the unstable branches Q, W, and Y respectively. Note that Q and Y are no longer degenerate.

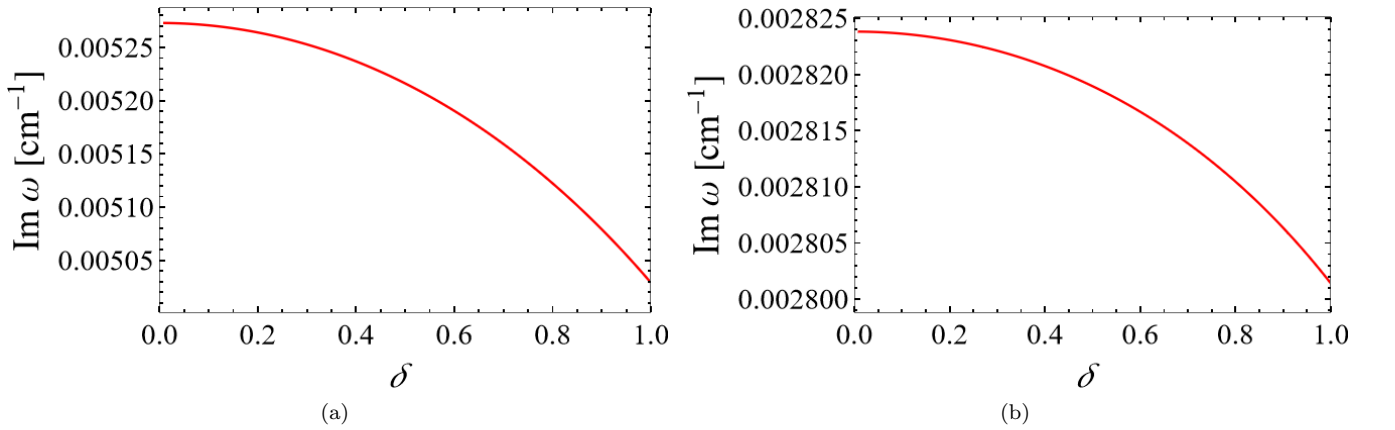


FIG. 13. The linear growth rates for mode W studied as functions of the degree of anisotropy δ . (a) at the resonance peak ($\bar{g} = 0.512$) and (b) at roughly half the peak amplitude ($\bar{g} = 0.51$).

VI. ACKNOWLEDGEMENT

J.L. thanks Taiki Morinaga for introducing this field of research to him and providing well constructed basic codes for dispersion relation analysis. This work is par-

tially supported by Grants-in-Aid for Scientific Research (21H01083) and the Grant-in-Aid for Scientific Research on Innovative areas “Unraveling the History of the Universe and Matter Evolution with Underground Physics” (19H05811) from the Ministry of Education, Culture,

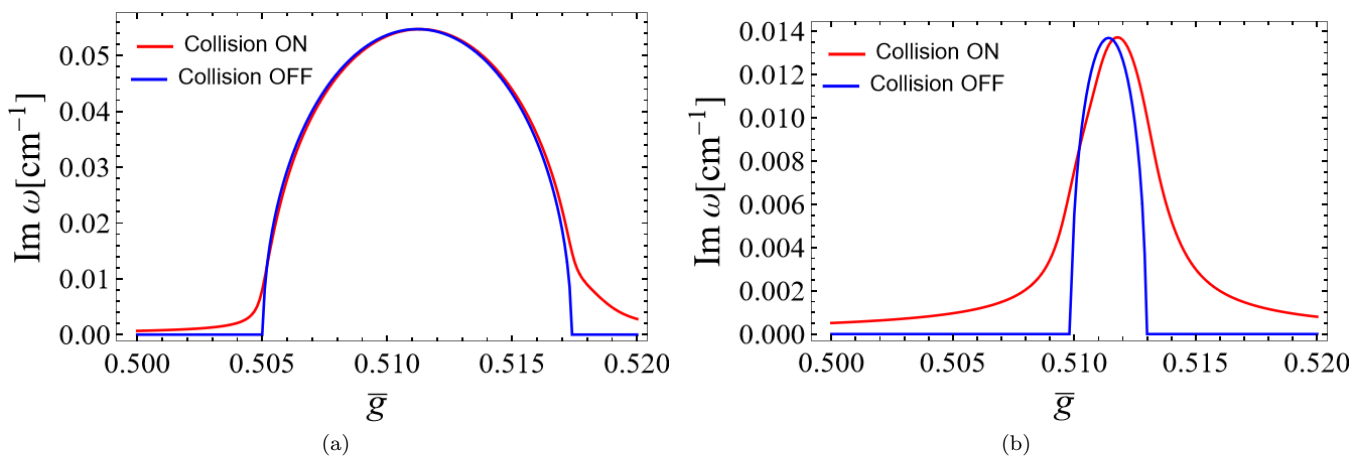


FIG. 14. The linear growth rates as functions of \bar{g} for anisotropic backgrounds with an ELN crossing. The collision term is either turned on (red) or off (blue). (a): $\delta = 1$ and $\bar{\delta} = 0.08$ and (b): $\delta = 1$ and $\bar{\delta} = 0.095$.

Sports, Science and Technology (MEXT), Japan. M.Z. is supported by the Japan Society for Promotion of Science (JSPS) Grant-in-Aid for JSPS Fellows (Grants No. 22J00440) from the Ministry of Education, Culture, Sports, Science, and Technology (MEXT) in Japan.

S.Y. is supported by Institute for Advanced Theoretical and Experimental Physics, Waseda University, and the Waseda University Grant for Special Research Projects (project No. 2022C-140).

-
- [1] J. Pantaleone, Dirac neutrinos in dense matter, *Phys. Rev. D* **46**, 510 (1992).
- [2] G. Sigl and G. Raffelt, General kinetic description of relativistic mixed neutrinos, *Nuclear Physics* **406**, 423 (1993).
- [3] H. Duan, G. M. Fuller, and Y.-Z. Qian, Collective neutrino oscillations, *Annual Review of Nuclear and Particle Science* **60**, 569 (2010), <https://doi.org/10.1146/annurev.nucl.012809.104524>.
- [4] S. Chakraborty, R. Hansen, I. Izaguirre, and G. Raffelt, Collective neutrino flavor conversion: Recent developments, *Nuclear Physics B* **908**, 366 (2016), neutrino Oscillations: Celebrating the Nobel Prize in Physics 2015.
- [5] I. Tamborra and S. Shalgar, New developments in flavor evolution of a dense neutrino gas, *Annual Review of Nuclear and Particle Science* **71**, 165 (2021), <https://doi.org/10.1146/annurev-nucl-102920-050505>.
- [6] S. Richers and M. Sen, Fast flavor transformations (2022).
- [7] T. Morinaga, Fast neutrino flavor instability and neutrino flavor lepton number crossings, *Phys. Rev. D* **105**, L101301 (2022).
- [8] S. Abbar, H. Duan, K. Sumiyoshi, T. Takiwaki, and M. C. Volpe, On the occurrence of fast neutrino flavor conversions in multidimensional supernova models, *Phys. Rev. D* **100**, 043004 (2019).
- [9] H. Nagakura, T. Morinaga, C. Kato, and S. Yamada, Fast-pairwise collective neutrino oscillations associated with asymmetric neutrino emissions in core-collapse supernovae, *The Astrophysical Journal* **886**, 139 (2019).
- [10] M. Delfan Azari, S. Yamada, T. Morinaga, H. Nagakura, S. Furusawa, A. Harada, H. Okawa, W. Iwakami, and K. Sumiyoshi, Fast collective neutrino oscillations inside the neutrino sphere in core-collapse supernovae, *Phys. Rev. D* **101**, 023018 (2020).
- [11] S. Abbar, H. Duan, K. Sumiyoshi, T. Takiwaki, and M. C. Volpe, Fast neutrino flavor conversion modes in multidimensional core-collapse supernova models: The role of the asymmetric neutrino distributions, *Phys. Rev. D* **101**, 043016 (2020).
- [12] T. Morinaga, H. Nagakura, C. Kato, and S. Yamada, Fast neutrino-flavor conversion in the preshock region of core-collapse supernovae, *Phys. Rev. Res.* **2**, 012046 (2020).
- [13] R. Glas, H.-T. Janka, F. Capozzi, M. Sen, B. Dasgupta, A. Mirizzi, and G. Sigl, Fast neutrino flavor instability in the neutron-star convection layer of three-dimensional supernova models, *Phys. Rev. D* **101**, 063001 (2020).
- [14] S. Abbar, Searching for fast neutrino flavor conversion modes in core-collapse supernova simulations, *Journal of Cosmology and Astroparticle Physics* **2020** (05), 027.
- [15] F. Capozzi, S. Abbar, R. Bollig, and H.-T. Janka, Fast neutrino flavor conversions in one-dimensional core-collapse supernova models with and without muon creation, *Phys. Rev. D* **103**, 063013 (2021).
- [16] H. Nagakura, A. Burrows, L. Johns, and G. M. Fuller, Where, when, and why: Occurrence of fast-pairwise collective neutrino oscillation in three-dimensional core-collapse supernova models, *Phys. Rev. D* **104**, 083025 (2021).
- [17] A. Harada and H. Nagakura, Prospects of fast flavor neutrino conversion in rotating core-collapse supernovae, *The Astrophysical Journal* **924**, 109 (2022).
- [18] R. Akaho, A. Harada, H. Nagakura, W. Iwakami, H. Okawa, S. Furusawa, H. Matsufuru, K. Sumiyoshi, and

- S. Yamada, Protoneutron star convection simulated with a new general relativistic boltzmann neutrino radiation-hydrodynamics code (2022).
- [19] J. D. Martin, J. Carlson, V. Cirigliano, and H. Duan, Fast flavor oscillations in dense neutrino media with collisions, *Phys. Rev. D* **103**, 063001 (2021).
- [20] G. Sigl, Simulations of fast neutrino flavor conversions with interactions in inhomogeneous media, *Phys. Rev. D* **105**, 043005 (2022).
- [21] L. Johns and H. Nagakura, Self-consistency in models of neutrino scattering and fast flavor conversion, *Phys. Rev. D* **106**, 043031 (2022).
- [22] S. Shalgar and I. Tamborra, Change of direction in pairwise neutrino conversion physics: The effect of collisions, *Phys. Rev. D* **103**, 063002 (2021).
- [23] C. Kato, H. Nagakura, and T. Morinaga, Neutrino transport with the monte carlo method. ii. quantum kinetic equations, *The Astrophysical Journal Supplement Series* **257**, 55 (2021).
- [24] H. Sasaki and T. Takiwaki, A detailed analysis of the dynamics of fast neutrino flavor conversions with scattering effects, *Progress of Theoretical and Experimental Physics* **2022**, 10.1093/ptep/ptac082 (2022), 073E01, <https://academic.oup.com/ptep/article-pdf/2022/7/073E01/44400755/ptac082.pdf>.
- [25] R. S. L. Hansen, S. Shalgar, and I. Tamborra, Enhancement or damping of fast neutrino flavor conversions due to collisions, *Phys. Rev. D* **105**, 123003 (2022).
- [26] C. Kato and H. Nagakura, Effects of energy-dependent scatterings on fast neutrino flavor conversions, *Physical Review D* **106**, 10.1103/physrevd.106.123013 (2022).
- [27] F. Capozzi, B. Dasgupta, A. Mirizzi, M. Sen, and G. Sigl, Collisional triggering of fast flavor conversions of supernova neutrinos, *Phys. Rev. Lett.* **122**, 091101 (2019).
- [28] L. Johns, Collisional flavor instabilities of supernova neutrinos (2021).
- [29] L. Johns and Z. Xiong, Collisional instabilities of neutrinos and their interplay with fast flavor conversion in compact objects, *Phys. Rev. D* **106**, 103029 (2022).
- [30] Y.-C. Lin and H. Duan, Collision-induced flavor instability in dense neutrino gases with energy-dependent scattering (2022).
- [31] S. Airen, F. Capozzi, S. Chakraborty, B. Dasgupta, G. Raffelt, and T. Stirner, Normal-mode analysis for collective neutrino oscillations, *Journal of Cosmology and Astroparticle Physics* **2018** (12), 019.
- [32] I. Izaguirre, G. Raffelt, and I. Tamborra, Fast pairwise conversion of supernova neutrinos: A dispersion relation approach, *Phys. Rev. Lett.* **118**, 021101 (2017).
- [33] Z. Xiong, L. Johns, M.-R. Wu, and H. Duan, Collisional flavor instability in dense neutrino gases (2022).
- [34] M. Zaizen and H. Nagakura, Simple method for determining asymptotic states of fast neutrino-flavor conversion, *arXiv e-prints*, arXiv:2211.09343 (2022), arXiv:2211.09343 [astro-ph.HE].
- [35] S. Shalgar and I. Tamborra, On the occurrence of crossings between the angular distributions of electron neutrinos and antineutrinos in the supernova core, *The Astrophysical Journal* **883**, 80 (2019).
- [36] S. Shalgar and I. Tamborra, Neutrino flavor conversion, advection, and collisions: The full solution (2022).